Natural Resources Canada | Ressources naturelles Canada

GEOLOGICAL SURVEY OF CANADA
OPEN FILE 7750

Electrical and electromagnetic data for permafrost characterization at Iqaluit International Airport, Nunavut

G.A. Oldenborger, A.-M. LeBlanc and W.E. Sladen

2015

Canada

GEOLOGICAL SURVEY OF CANADA
OPEN FILE 7750

Electrical and electromagnetic data for permafrost characterization at Iqaluit International Airport, Nunavut

G.A. Oldenborger, A.-M. LeBlanc and W.E. Sladen

2015

doi:10.4095/295978

This publication is available for free download through GEOSCAN (http://geoscan.nrcan.gc.ca/).

Recommended citation
Oldenborger, G.A., LeBlanc, A-M., and Sladen, W.E., 2015. Electrical and electromagnetic data for permafrost characterization at Iqaluit International Airport, Nunavut; Geological Survey of Canada, Open File 7750, 43 p. doi:10.4095/295978

Publications in this series have not been edited; they are released as submitted by the author.

SUMMARY

Iqaluit International Airport presently suffers from instabilities and subsidence along its runway, taxiways and apron. In particular, asphalt surfaces are significantly impacted by settlement and cracking These instabilities may be related to permafrost, permafrost degradation and associated drainage conditions. This Open File reports on electrical and electromagnetic geophysical data collected and processed by the Geological Survey of Canada at the Iqaluit International Airport as part of the Land-Based Infrastructure Project within the Climate Change Geoscience Program. Galvanic and capacitive electrical resistivity surveys, along with low induction number electromagnetic measurements, were performed over selected areas within the airport boundary and in the near vicinity to assist with permafrost characterization and to investigate active permafrost processes. The recovered electrical resistivities suggest distinct electrical signatures for different terrain units and sediment types, and for ice-rich material including ice wedges. Even with continuous permafrost and cold permafrost temperatures, the resistivity models reveal anomalously conductive material at depth that is not obviously correlated to mapped surficial sediments. The anomalous regions are correlated with localized settlement problems and downward multi-season displacement derived from D-InSAR. The geophysical surveys also exhibit features indicative of seasonal freezing of localized groundwater beneath airport infrastructure and variable active layer thickness under infrastructure that is thicker than for undeveloped ground.

TABLE OF CONTENTS

INTRODUCTION

Permafrost and associated ground ice can significantly affect land-based infrastructure through influence on ground stability and drainage patterns. As such, geoscience information contributing to permafrost characterization is critical for understanding risks to roads and airports which are vital to economic development in Canada's North. To this end, the Geological Survey of Canada (GSC) established the Land-Based Infrastructure project within the Climate Change Geoscience Program with the objective of providing geoscience data and expertise to reduce risks and aid in adaptation solutions for Northern Canada. One component of this activity, in collaboration with the Canada-Nunavut Geoscience Office (CNGO), is the application of geophysical methods to aid in mapping and characterization of permafrost conditions at the Iqaluit International Airport.

Iqaluit International Airport has experienced a variety of geotechnical problems over its history. Recurring settlement, deformation and noticeable damage have required several campaigns of resurfacing and reparation (Larochelle and Haché 1991; Knapik and Hanna 1998). At least one case of recent deterioration requiring significant repair was concluded to result from excessive permafrost degradation associated with drainage engineering (Dietrich and Mitchell 2012). Detailed and extensive knowledge of subsurface conditions, including permafrost, is necessary for informed and cost-effective management of airport infrastructure and facilities.

The unique electrical properties of frozen ground make electrical and electromagnetic geophysics a potential tool for characterization of permafrost terrain (e.g., Scott and Hunter 1977; Hoekstra 1978; Sartorelli and French 1982; Scott et al. 1990; Hauck et al. 2001; Ross et al. 2007; Fortier et al. 2008; Sladen et al. 2009; Oldenborger et al. 2012; Hauck 2013; You et al., 2013; Supper et al. 2014; Wolfe et al. 2014). Electrical and electromagnetic data have been collected over runway, taxiway and apron portions of Iqaluit International Airport, and over sections of natural ground in the vicinity of the airport. Data collection was both regional and targeted based on existing problematic areas, knowledge of surficial geology and observations of permafrost features. The objective was to determine if distinct geophysical signatures could be attributed to sediment or terrain type, and if electrical resistivity models could prove useful for understanding permafrost conditions causing infrastructure damage by reliably mapping features such as ice-bearing sediment, ice-rich regions or thaw zones.

STUDY AREA

Iqaluit International Airport (YFB) is located in Iqaluit, Nunavut at the head of Frobisher Bay on Baffin Island (Figure 1). It is built on flat terrain surrounded by hills and rocky plateaus of the Precambrian Shield within the continuous permafrost zone. The surficial geology has been mapped by Allard et al. (2012). The present-day Runway 17/35 was originally constructed in part in 1942 followed by a runway extension in 1948. The 1942 portion of Runway 17/35 was built on glaciomarine delta deposits composed of sand, silt, boulders and gravel; the 1948 portion was built on glaciofluvial outwash, bedrock and fill material (Figure 2). Alluvial channels and lacustrine deposits are present under the embankments of taxiways, aprons and access roads, and till and marine sediments are observed in the immediate vicinity. These smaller-scale deposits may play a critical role in determining permafrost conditions due to their relationship with water channelling (alluvial sediments) or excess ice (fine-grained sediments); knowledge of their subsurface extent is important.

The mean annual ground temperature for southern Baffin Island is −5 to −10ºC, with low to high occurrence of ground ice, including ice wedges and massive ice bodies (Heginbottom et al. 1995; Allard et al. 2012). As part of GSC/CNGO activities, thermistor cables were installed in 2010 and 2011 in the natural terrain and within the embankment infrastructures at YFB (LeBlanc et al., 2013). The permafrost temperature recorded in natural terrain is approximately −5ºC at a depth of zero annual amplitude of 14 m with an active-layer thickness of 1.5 m. Active-layer thickness is locally observed to be variable and can be in excess of 4 m under paved infrastructure (Larochelle and Haché 1991; Dietrich and Mitchell 2011).

GEOPHYSICAL METHODS

The primary physical parameter governing the low-frequency electrical and electromagnetic geophysical response is the electrical resistivity (the inverse of electrical conductivity). In most near-surface geologic environments, controlling factors on the bulk electrical resistivity of rocks and sediments are the amount of pore fluid, the connectivity of the pore fluid, and the availability and mobility of charge-carrying ions. Electrical resistivity can often be considered as a proxy for material type (sedimentology or lithology) inasmuch as the material type affects the porosity, water retention, and the availability and behaviour of ions in solution and exchangeable cations (e.g., McNeil 1980a; Klein and Santamarina 2003).

Permafrost can have a strong and complicating influence on electrical resistivity because low temperatures reduce the mobility of charge-carrying ions and the freezing of water greatly reduces the availability and connectivity of pore fluid for electrolytic conduction (King et al. 1988). Consequently, resistivity is observed to increase gradually down to the freezing point and increase dramatically for temperatures below freezing (Figure 3).

At low ground temperatures, the unfrozen water content may be reduced to a point where there is little contrast in resistivity between frozen sediment or massive ice or even air (Hoekstra et al. 1975). Nevertheless, cryotic sediments with high salinity may contain appreciable unfrozen water content due to exclusion of salts and freezing point depression (Grimm et al. 2008). Similarly, cryotic fine-grain materials may contain appreciable unfrozen water content due to suction forces, to the point where permafrost may be quite conductive for certain material types (e.g., Ross et al. 2007).

In permafrost terrain, measurements of electrical resistivity can generally be used to infer some combination of the pore-fluid conductivity and the moisture content, or similarly, the material type and the amount of frozen/unfrozen water. As such, electrical and electromagnetic geophysics can be applied in an attempt to map material type and to characterize occurrence of ice-bearing permafrost, thaw zones and thermophysical transitions underground.

Data Acquisition

In early August 2010, preliminary galvanic and capacitive electrical resistivity data were collected in the area around YFB, but not on runway or taxiway structures. In late July 2011, capacitive resistivity surveys were performed along Runway 17/35 and Taxiway Alpha (Taxi A). In July and August 2012, electrodes were installed along Taxi A and resistivity data were collected in early August 2012 and subsequently in November 2012, July 2013, October 2013, February 2014 and August 2014 (although only the initial data set is presented herein). An addtional galvanic resistivity survey was collected along the north side of Taxi A in August

2014. Complimentary low induction number electromagnetic data were acquired over portions of Runway 17/35 and Taxi A in February 2012 and again in July and August 2012. Figure 4 shows the location of data sets to be discussed in turn in this Open File along with locations of boreholes along the runway and Taxi A.

Galvanic Resistivity Data

The galvanic resistivity (GR) survey involves injection of current into the ground via contact with a pair of current electrodes (Figure 5). The potential distribution is then measured across many pairs of voltage electrodes and an electrical resistivity model is constructed that adequately honours the data (e.g., Loke et al. 2013). Data were collected using a 48-electrode resistivity meter (IRIS Syscal R1+ Switch) with variable electrode spacings and 0.3 m stainless steel electrodes or buried stainless steel mesh electrodes.

The initial processing step involves thorough examination of the data along with field notes; obvious outliers and data associated with any non-contact electrodes are eliminated along with extremely low-voltage data and data with poor repeatability and/or very high chargeability. Survey geometry is assigned which involves translation to a prescribed coordinate system and assignment of topography if required. In the case of 2D GR data collected with a multicore cable, processing is done in terms of survey lines and distance along the cable (along the ground). For each line, static global positioning system (GPS) coordinates were acquired for at least the first and last electrodes and also any important positions along each line using a NovAtel Smart V receiver with wide area augmentation for which a reference station is located in Iqaluit.

Capacitive Resistivity Data

In a capacitive resistivity (CR) survey, current is generated in the ground via coupling of an alternating current across a transmitter-earth capacitor (Kuras et al. 2006). Similarly, voltage is measured via coupling of the resulting potential field across an earth-receiver capacitor. A CR system is non-contacting and allows for acquisition of data where physical contact with the ground via electrodes is prohibitive, such as along roads or where contact resistance with the ground is prohibitively high such as for ice or very dry soils.

CR data were collected with an OhmMapper system developed by Geometrics Ltd. using one transmitter and five receivers (Groom 2008). The OhmMapper uses line antennas for capacitive coupling and surveys were executed with either 5 m or 10 m antenna lengths (or both) with multiple passes at variable transmitter-receiver spacings (Figure 6). OhmMapper data are conventionally considered analogous to those from a GR survey with an in-line dipole-dipole geometry and a dipole length equal to the antenna length, but certain operating conditions must be satisfied (e.g., Oldenborger and LeBlanc 2013).

The initial processing step is de-spiking of the voltage data followed by a low-pass filter. Survey geometry is defined either manually or via integrated GPS positions and then the time-sampled data are averaged to a constant nominal electrode spacing equal to half of the antenna length. Averaged voltage data are converted to measurements of apparent resistivity using a line-antenna geometric factor (Groom 2008). The apparent resistivity data are then corrected for an effective dipole length of 80% of the antenna length to allow for inversion using a 4-point GR electrode model (Oldenborger and LeBlanc 2013).

Both the GR data and the corrected CR data are used for electrical resistivity imaging (ERI) of the subsurface via the iteratively re-weighted least squares inversion method of Loke et al. (2003). The same inversion settings have been applied to the GR and CCR data sets. Data with greater than 10% misfit are re-weighted to reduce the effect of outliers and a large Ekblom perturbation of 0.5 is used to approximate a "soft" L_1 norm on the model that results in both smooth and blocky features to some extent (Farquharson and Oldenburg, 1998). Logarithmic transformations are used on both the data and the model, and no bounds are placed on the recovered model values. The model cell sizes are set at one-half (horizontal) by one-quarter (vertical) of the (nominal) electrode spacing and represent an over parameterization of the model such that cell size should not significantly affect inversion results. The regularization parameter is cooled from 0.30–0.06 and convergence was defined as less than 5% change in the data misfit or a prediction error below 3% which is on par with the maximum accepTable repeatability of the GR data (although experimental noise may often exceed observed repeatability, particularly for CR data). Model regularization is generally set to recover models with 2:1 horizontal-to-vertical smoothness and a locally-determined reference model is applied with a regularization weight equal to the smallest value of the regularization parameter in the cooling schedule. The recovered models are relatively robust to small changes in inversion settings, although different noise levels between the GR and CR data result in different convergence behaviours; different levels of convergence result in different amounts of final damping and different resolution.

Model Uncertainty

The resistivity models obtained via inversion of the GR and CR data are subject to limitations in resolution (e.g., Oldenburg and Li 2005). For 2D surface surveys, model uncertainty or resolution loss can be approximated by the linearized resolution matrix. However, since the resolution matrix is large, it is customary to examine only its diagonal elements or properties (e.g., Friedel 2003). Furthermore, since it is linearized, the resolution matrix exhibits a strong dependence on the final model regardless of its veracity (e.g., Oldenborger and LeBlanc 2013). Alternatively, the depth of investigation (DOI) captures the non-linear nature of the inversion and is not subject to choice of final model as is the resolution measure (Oldenburg and Li 1999). The DOI also tends to capture regions of severe non-uniqueness: areas where resolution is high, but the actual value of the recovered model is very sensitive to starting conditions (Oldenborger et al. 2007).

Although useful, the DOI suffers from ambiguity associated with the amount of damping applied during the inversion (Deceuster et al. 2014; Oldenborger 2014). Unless the weighting associated with the reference model is made particularly strong, the smallness-to-smoothness ratio can be insufficient to allow for reliable application of a simple-difference DOI and some form of variable reference model is required combined with a cross-correlation analysis (Oldenburg and Li 1999). A good indication of sufficient smallness is that the DOI index equals unity at model boundaries. As such, scaling of the DOI as suggested by (Marescot et al. 2003) can be detrimental—if the DOI does not reach unity, it is likely that there is not enough smallness in the solution to warrant application of the DOI (Miller and Routh 2007). Furthermore, if one inadvertently scales by a value higher than unity, the scaled DOI can be misleadingly permissive.

To address limitations of both the resolution matrix and the DOI, the two measures can be combined. Figure 7 shows the resolution matrix diagonals and DOI for a typical GR inversion.

Both the resolution and DOI suggest regions of uncertainty that differ significantly from the homogeneous case. In general, the contour level of 0.5% the maximum resolution per area yields a resolution limit that is in good agreement with the DOI. However, the DOI highlights at least two areas with relatively high resolution that are subject to model non-uniqueness. A limit that honours the shallower of the two measures represents a conservative estimate of the depth of model reliability. A DOI with insufficient smallness results in an overly permissive limit as does the resolution matrix computed for an inversion without a reference model, for which a more appropriate cut-off level would need to be determined.

EM31 Data

Low induction number electromagnetic instruments measure the secondary magnetic field response that is directly proportional to the electrical conductivity of homogeneous ground for a given operating range (McNeil 1980b; Beamish 2011). In the case of layered or heterogeneous ground, the measured quantity is termed "apparent conductivity" and represents a conductivity-weighted average of the primary field intensity (Sartorelli and French 1982).

Data at YFB were acquired with a Geonics EM31 terrain conductivity meter. The EM31 can be operated with horizontal or vertical magnetic dipole orientations resulting in depths of exploration of approximately 3 m and 6 m respectively. However, the depth response of the EM31 is nonlinear and measurements represent integrated values; for a typical configuration of vertical dipoles (horizontal co-planar coils) at 1 m height above the ground surface, approximately 50% of the cumulative measured secondary magnetic field comes from the top 3 m of homogeneous ground and approximately 70% from the top 6 m. More generally, vertical dipole data can be regarded as "deep" whereas horizontal dipole data can be regarded as "shallow."

EM31 data were collected as point measurements along survey transects. Simultaneous GPS positions were recorded such that neither points nor transects were necessarily regularly spaced, although the surveys followed linear infrastructure. The data were calibrated using a constant shift parameter to establish a baseline minimum conductivity of 0.1 mS/m or 10 kΩm over the igneous bedrock at YFB (Palacky, 1988). The data were de-spiked to remove the response associated with known fuel pipes under the airport pavement. Station reoccupations were used to check for measurement drift. Operational constraints of working on an active airstrip meant that insufficient data were collected for a full drift correction. Nevertheless, the drift measurements can be used to estimate approximate repeatability errors of less than 0.5 mS/m or 200 Ωm. Point measurements of apparent conductivity are interpolated to produce maps of apparent conductivity using linear interpolation and a 50 m search radius with a minimum of 8-point support followed by conversion to log-transformed apparent resistivity.

RESULTS

2010 CR and GR Surveys

CR data were collected in early August 2010 along unsurfaced roads to the southwest of the airport boundary (sites A3 and A7) and over apron infrastructure with known issues of subsidence (site A11) using 5 m antenna lengths. Complementary GR data were collected at site

A7 and additional GR data were collected over a region of suspected ice wedge prevalence (site A10).

The CR resistivity model for site A03 is shown in Figure 8. For this and all subsequent resistivity models, the limit of model reliability is represented as the shallower of the 0.5% maximum resolution per area and the 0.2 DOI index. The model is interpreted to represent sand and gravel of 1000–3000 Ωm associated with the mapped glaciomarine deltaic unit at surface (GMd, Figures 2 and 4). Although distinct imaging of a thin active layer (less than 1.5 m thick) is difficult with these data, we interpret it to be manifest as the slight transition to lower resistivities at the surface of the model, particularly to the northwest. Below depths of approximately 5 m, the model predicts material with an electrical resistivity as low as 10–30 Ωm which is remarkably low for cold, continuous permafrost and may represent fine-grained marine sediments with potentially saline pore water. A transition to finer grained material is likely required to achieve the observed resistivity contrast as opposed to only a strong pore-water transition within the same glaciomarine deltaic sediments. Reliable interpretation at depth is hampered by loss of current penetration into the conductive unit as evidenced by the limit of reliability. Furthermore, a grounded metallic fence runs parallel with the A03 survey line which would contribute to a conductive artefact in the model (although this deep conductive material is present at sites without cultural interference).

Figure 9 shows the CR and GR resistivity models for nearby site A07. As discussed by Oldenborger and LeBlanc (2013), an effective dipole length correction achieves maximum consistency between the collocated GR and CR resistivity models. Again, a thin active layer is interpreted to appear as the transition to lower resistivities at the very surface of the models. The interpreted active layer thickens near the intersection of survey lines A07 and A07x and at the middle of survey line A07x which is a marshy area with ponded water. The marine littoral sediments (Mn, Figures 2 and 4) are largely silty to gravelly sand consistent with the observed resistivity of 1000–3000 Ωm along line A07. The till blanket at the north end of line A07 (Tb, Figures 2 and 4) has a silty-sand matrix and appears more conductive than the marine sediments (500–1500 Ωm). Bedrock topography in the region is observed to be quite variable and the resistive anomalies at 10–15m depth at the southern end of A07 are interpreted to be indicative of bedrock highs. Reliability at this depth is limited and a strong versus moderate resistor, or the location of the bedrock contact cannot be distinguished in this case. At intermediate depths, the model predicts a conductive material (10–30 Ωm) similar to that at site A03 that is not identified on surficial maps, but may have limited surficial expression (line position 450–475 m) One possibility, given the interpreted marine limit in the region (Figure 2) is fine-grained marine sediments with potentially saline pore water. Line A07x differs from Line A07 in that a strongly resistive signature (5000–8000 Ωm) is recovered for the mapped marine sediments. This feature is interpreted to be ice-rich sediment underlying the marshy region along the east side of Sylvia Grinnell road.

Figure 10 shows the GR resistivity model for site A10. This site has a high occurrence of frost cracks and ice-wedge features as mapped by Allard et al. (2012). The model recovers a thin active layer overtop of the mapped glaciomarine deltaic sands and gravels (800–2000 Ωm). The resistive anomalies at 7, 20, 65, 87, 100, 135, 158, and 175 m line position all coincide with surficial furrows forming part of the surface polygonal network (Figures 2 and 4). In particular, the strongest anomaly at 87 m represents the intersection of multiple furrows and is interpreted to be ice-cored (8000–10000 Ωm). Although at relatively low resolution, this experiment demonstrates the ability of ERI to map ice wedge occurrence. Below the glaciomarine deltaic

sands and gravels, there is a transition to more conductive material identified as fine sand in nearby borehole observations (Mathon-Dufour, 2014; Leblanc et al., 2015), but resolution is low at this depth.

Figure 11 shows the CR apparent resistivity data collected for site A11 over part of the YFB apron that was experiencing surficial cracking. There is no obvious representation of the mapped crack features in the apparent resistivity data. The most obvious feature is a linear conductive anomaly that strikes to the northeast and appears to dip to the northwest. Given the magnitude and linearity of this feature, it is likely related to apron infrastructure. Figure 12 shows the CR resistivity models for site A11. There are no obvious resistivity anomalies associated with surface cracking. However, the small surface resistivity anomalies at 70, 80 and 30 m on west to east lines respectively are coincident with mapped cracks, but these features have no depth persistence.

2011 CR Surveys

CR data were collected in late July 2011 along Runway 17/35, Taxi A and Taxi B using 10 m antenna lengths. The CR resistivity model for the runway is shown in Figure 13 along with schematic stratigraphy derived from cored boreholes DH13-06 and DH13-09 (Figure 4) described by Mathon-Dufour (2014). The high resistivity material to the northwest from approximately 1000 m line position is interpreted as bedrock (8000–20000 Ωm) which outcrops on either side of the runway. The moderately resistive feature at the bay-end of the runway near −1200 m line position may be related to the path of the previous runway or may be a manifestation of a depositional transition in the glaciomarine sediments. A boundary at approximately 4 m depth is interpreted to be the base of observed sand and gravel, a combination of embankment fill over glaciomarine or glaciofluvial sediments (800–3000 Ωm). The surface layer becomes more resistive over the interpreted bedrock, perhaps indicative of predominantly rockfill embankment. Of particular note is the conductive anomaly (20–300 Ωm) observed from approximately −300–500 m line position. This anomaly is distinct from model artefacts resulting from culture (likely buried cables) at −1000 and 550 m line position, for example, that are characterized by low model reliability resulting from severe non-uniqueness. The conductive anomaly located near 790 m line position occurs in the vicinity of several mapped lacustrine units (Figure 2). Lacustrine sediments either at depth or off-line represent a potential source for this conductive anomaly, but no similar association is apparent for the other observed anomalies.

The CR resistivity model for Taxi A is shown in Figure 14 with schematic stratigraphy from off-line cored boreholes (DH13-02 and DH13-10) and an air-drilled borehole (DH11-07) with a thermistor cable installation (LeBlanc et al. 2013; Mathon-Dufour 2014). A surficial conductive anomaly (50–200 Ωm) extends to approximately 4 m depth from −85 to 15m line positon and correlates well with mapped lacustrine silts (Figure 4) and observations in DH13-02. Resistive embankment is likely present overtop of the lacustrine silts, but neither it nor the active layer are recovered by the model due to limited surficial resolution associated with 10 m antennas. On either side of the surficial conductive feature, the ground is relatively resistive (800–1500 Ωm) corresponding to mapped glaciofluvial and glaciomarine deltaic deposits (Figure 4). There is a potential ice-rich zone at approximately −50 m line position (800–1500 Ωm). There is another well-defined conductive anomaly (5–50 Ωm) below approximately 4m depth extending from −150 to 0 m line position; the relation of this anomaly to the mapped lacustrine sediments is unknown as it continues beneath the glaciofluvial and glaciomarine map units. Conductive

material is also observed beneath the glaciomarine sediments to the east, but reliability of this portion of the model is poor.

The CR resistivity model for Taxi B is shown in Figure 15. The model is significantly more resistive than either the runway or Taxi A. The survey line extends across a mapped alluvial channel that is observed as an area of elevated resistivity (3000–10000 Ωm) below depths of 3 m from approximately from −10 to 60 m line position. High resistivities (1000–8000 Ωm) are also observed for the rest of the survey line over areas mapped as glaciomarine deltaic. The most northern portion of the survey line extends over or near a mapped lacustrine unit, but no evidence of this is observed in the resistivity model.

Taxiway Alpha GR Surveys

Along Taxi A, a one-time survey using 48 removable electrodes at 5 m spacing (Figure 4, L5) was conducted in late July 2012 prior to a survey in early August using a permanent subsurface installation of 72 electrodes at 2 m spacing (Figure 4, L2). Installation is discussed in detail by Oldenborger et al. (2014). In August 2014, an additional survey using 48 removable electrodes at 2 m spacing was conducted along the north shoulder of Taxi A with the objective of acquiring GR data representative of bedrock. Figure 16 shows the GR resistivity models for Taxi A that, in general, have higher resolution than the previous Taxi A CR counterparts with 10 m antenna length. Bedrock is clearly imaged along the northern line (4000–16000 Ωm) along with the embankment, the resistivity of which is reduced by the presence of the active layer (Figure 16c). The bedrock signature in the L5 and L2 models is weak due to inherent resolution loss at depth and current concentration within the conductive overburden. Nevertheless, the resistivity models combined with the borehole observations indicate significant subsurface bedrock topography. The L5 and L2 models are dominated by conductive material with some apparent internal structure. From approximately 85 to 140 m line position (L2) and from 2–6 m depth, a conductive feature (15–30 Ωm) is well-correlated with the mapped lacustrine deposits (Figures 2 and 4). Below 6 m depth, the L2 GR model suggests that the lacustrine deposits may be layered or deposited over previous material of higher resistivity (50–200 Ωm) with similar spatial extent. Similar to the CR model (Figure 14), there is another well-defined and more extensive conductive anomaly (1–30 Ωm) below the glacial and lacustrine deposits that correlates with the known area of differential settlement extending beyond the mapped lacustrine sediments. The same decrease in resistivity with depth is observed in boreholes BH1 and BH2 in July 2013 (Oldenborger et al. 2014). At the surface of the L2 and L5 models, there is a thickening wedge of resistive material (2000–10000 Ωm) observed to the west that is interpreted as ice-rich glaciomarine sand and gravel over a local stream and historical wet area (Figure 4, Short et al. 2014).

2012 EM31 Surveys

The winter and summer EM31 data are shown in Figures 17 and 18 respectively. Data were acquired at point locations that are different for the two datasets. Given the sometimes sparse and localized nature of the data set, there may be gridding artefacts in the mapped apparent resistivities. There is also some indication of cross-line levelling errors (such as contours that appear stair-stepped, or change direction rapidly at a line location). As such, the apparent

conductivity maps should be interpreted in light of the actual data locations, and off-line information must be acknowledged as interpolated.

The EM31 data capture the transition from bedrock to glaciofluvial deposits at the northern end of the runway (Figure 17). Most strikingly, the EM31 data identify an area of anomalously high apparent conductivity around the intersection of Runway 17/35 and Taxi A. The anomaly is characterized by apparent resistivities of 50–100 Ωm in both winter and summer. The extent of the conductive anomaly increases with depth, suggestive that the source is not a surficial feature. The anomaly extends over portions of Runway 17/35 and Taxi A where anomalously low resistivities are also observed in the CR and GR data (Figures 13, 14 and 16). Furthermore, the EM31 conductive anomaly is correlated with patterns of ground displacement as measured by D-InSAR (Short et al. 2014), but both the EM31 anomaly and the D-InSAR displacement pattern extend beyond the mapped lacustrine sediments (Figures 2 and 4).

In the winter data set, there is a highly resistive feature crossing the apron in a north-south direction that follows the trend of a mapped alluvial channel (Figures 2 and 4). The extent of the resistive anomaly appears to decrease in extent with depth, suggesting that the source is shallow in nature. This observation is consistent with an ice-rich alluvial system (i.e., sands and gravels with high porosity and a large amount of seasonally frozen water).

The change in apparent resistivity from winter to summer is shown in Figures 19 and 20. In general, there is a moderate increase in apparent resistivity from summer to winter as would be expected for decreased temperatures and freezing of the active layer. However, the region associated with the conductive anomaly demonstrates very little change in apparent resistivity. In contrast, the region of the apron associated with the resistive anomaly is co-located with an area of a significant increase in apparent resistivity in the winter. Such a change would occur if water in the alluvial system is only seasonally frozen. In other words, the EM31 data suggest that groundwater may be active under the apron in the summer season. Similar winter increases in apparent resistivity are observed beneath Taxi A and the runway and may be associated with active summer groundwater within the mapped glaciofluvial sediments.

There is anecdotal evidence that significant cultural material (including vehicle parts and fuel drums) may exist in the subsurface beneath the runway and/or taxiways, in addition to many known infrastructures such as fuel pipes or electrical wiring. Negative swings in the apparent conductivity were observed only over known buried infrastructure and the in-phase EM31 response was observed to spike over infrastructure such as lights, but no response indicative of more extensive subsurface metal was observed. In fact, the in-phase response seems to be a conductivity-coupled response (not shown) and not a magnetic response associated with potential buried metal. An in-phase response that is spatially correlated to conductivity suggests potential violation of the low-induction number condition (Beamish, 2011). In general EM31 apparent resistivities should be considered as relative, not absolute, values such that general interpretations are not jeopardized.

DISCUSSION

Table 1 and Figure 21 provide the observed distribution of model resistivities for the YFB region on a site-by-site basis. The observed resistivities are classified based on the correlation to the mapped surficial sediments (Figures 2 and 4). Figure 22 illustrates the same distribution where the observed resistivities are both ordered and grouped based on common map units (Allard et al. 2012). However, map units are stratigraphic in nature and may not represent unique

sediment types, grain size distributions, or ground-ice occurrence. This is evidenced by only a partial distinction of mapped units based on electrical resistivity. For example, it is difficult to distinguish between glaciomarine deltaic sediments (GMd) and glaciofluvial sediments (GFp) and, in some cases, nearshore sediments (Mn) due to their generally common composition of sand and gravel. Similarly, ice-rich glaciomarine deltaic sediments (GMd) are electrically similar to alluvial sediments or even bedrock. Nevertheless, mapped stratigraphic units can be partially distinguished based on electrical resistivity. In addition, the anomalously low observed resistivities are not obviously correlated to any mapped surficial deposits, are largely consistent across sites, and are largely distinct from other map units.

Using surficial mapping descriptions (Allard et al. 2012) and borehole observations (Mathon-Dufour 2014), the observed resistivities can be further grouped based on interpreted material type as shown in Figure 23. There are distinct (gradational) electrical signatures for the different groupings (although this trend is dictated to some degree by the interpreted material type). The source of the anomalously low resistivities is unknown. Observations while air-drilling suggest relatively homogeneous silt and sand below Taxi A, which alone would not typically account for the observed resistivity or the variations in resistivity.

Grain size distribution, water content and salinity measurements were performed on disturbed borehole cutting samples from DH11-07 on the shoulder of Taxi A (Table 2); the grain size distributions suggest an increase in sand with depth which would tend to reduce both the unfrozen water content and the available ions for electrolytic conduction. However, the limited number of water conductivity measurements indicate that salinity increases with depth, approaching 9 parts per thousand at 12 m depth (Table 2). Salinities approaching that of seawater have been reported in the vicinity at depths of 10 m (Knapik and Hanna 1998) consistent with the mapped marine limit (Figure 4). Due to salt exclusion during freezing, pore-water salinities approaching seawater will result in extremely elevated electrical conductivity of any unfrozen water content in addition to lowering the freezing point of the remaining water to several degrees below zero.

There is some overlap observed between the resistivity of the silty lacustrine deposits (Lv) and the unidentified conductive material (Figure 23) suggesting that there may be some genetic relation. This hypothesis is supported by historical observations of large amounts of surface water in the region between Runway 17/35 and Taxi A (Short et al. 2014). This water-rich region extends from the taxiway, across the runway and correlates with the overlapping conductive anomalies observed in both the EM31 data and the CR model for Runway 17/35. Similarly, evidence of the role of groundwater is observed in the EM31 data for which there is a large increase in apparent resistivity from summer to winter. These large increases in winter resistivity are correlated with known persistent settlement of the apron surface and are consistent with alluvial material and large amounts of seasonally frozen water.

For the experiments considered here, electrode spacing is generally too large to accurately capture the effect of the active layer which is typically a conductive anomaly for homogeneous ground in the summer months. This lack of resolution is exacerbated by the countering effect of resistive surficial material such as embankment or glaciofluvial sediments. If the active layer is entirely within the resistive surface layer, it will have the effect of reducing the summer bulk resistivity due to unfrozen water content. If the active layer extends below the resistive surface layer, it is likely indistinguishable from the lower more conductive ground.

Within the active layer, there may also be temperature dependence associated with the electrical resistivity that is independent of the effect of the phase change of water at freezing. For

electrolytic solutions, the low-temperature dependence of electrical resistivity can be approximated by a linear increase in resistivity with decreased temperature (e.g., Hayashi 2004). By extension, the same linear relationship can be applied to earth material dominated by electrolytic conduction in a linear fashion such as that predicted by Archie's Law for which bulk resistivity is directly proportional to fluid resistivity (e.g., Knight and Endres 2005). Theoretically, in a permafrost environment, a correction for temperature could be applied upwards from the thaw depth to normalize unfrozen resistivity to 0ºC. In the case of Taxi A, the temperature distribution is shown in Figure 24. Using the model of Hayashi (2004), the maximum correction would be a 17% increase in the recovered resistivity at the ground surface to compensate for July temperatures. The magnitude of the correction would decrease downwards to the thaw table. Below the freezing temperature, the effect of the reduction in available unfrozen water dominates any temperature effects in the remaining electrolytic solution and resistivity increases exponentially (e.g., King, 1977).

CONCLUSIONS

This Open File reports on electrical and electromagnetic geophysical data collected by the GSC at Iqaluit International Airport as part of the Land-Based Infrastructure Project within the Climate Change Program of Natural Resources Canada. Recovered resistivity models suggest distinct electrical signatures for most of the terrain types encountered which would allow for extensive geophysical characterization complimentary to landscape mapping, temperature data and shallow boreholes. The resistivity models also exhibit features indicative material type including ice-rich sediment and ice wedges. Several conductive anomalies are observed across YFB and the surrounding area which may be indicative of unidentified fine-grained material or large increases in pore-water salinity, both of which contribute to reduced resistivity and freezing point depression.

The observed conductive anomalies correlate across the different survey sites and survey types (GR, CR, EM31) and are correlated with D-InSAR displacement and known differential settlement of airport infrastructures. As such, low resistivity may serve useful as an indicator of infrastructure sensitivity. However, as both a modelled and proxy quantity, electrical resistivity models are subject to some interpretation and error. The results herein should be considered in the context of the other forms of permafrost assessment.

ACKNOWLEDGMENTS

This work was conducted as part of the Climate Change Geoscience Program of Natural Resources Canada in conjunction with the Canada-Nunavut Geoscience Office and was partly funded by the Canadian Northern Economic Development Agency's Strategic Investments in Northern Economic Development program. GR and CR data from 2010 were collected by G.A. Oldenborger with assistance from P. Gosselin, A.-S. Carbonneau, V. Mathon-Dufour, J. Doyon and S. Hatcher. CR data from 2011 were collected by M. Douma, A.-M. LeBlanc, and W.E. Sladen. EM31 data from 2012 were collected by G.A. Oldenborger, A.-M. LeBlanc and W.E. Sladen. GR data from 2012 and 2013 were collected by G.A. Oldenborger with assistance from A.-M. LeBlanc and W.E. Sladen. The authors thank J. Graham, J. Hawkins, K. Henderson and the management team at Iqaluit International Airport for site access and co-operation;

D. Mate and the Canada-Nunavut Geoscience Office for financial and in-kind contributions; M. Allard for helpful discussions on the Iqaluit area; and K. Brewer for critical review.

The electrical resistivity models and maps presented in this Open File are the result of iterative processing, filtering and multiple inversions. Neither the data nor the resistivity models are provided in the Open File release in digital format. Raw digital data, GPS data, and/or digital model files are freely available and may be obtained by contacting the author(s).

REFERENCES

Allard M., Doyon J., Mathon-Dufour V., LeBlanc A.-M., L'Hérault E., Mate D., Oldenborger G.A. and Sladen W. 2012. Surficial geology, Iqaluit, Nunavut. Geological Survey of Canada, Canadian Geoscience Map 64.

Beamish D. 2011. Low induction number, ground conductivity meters: A correction procedure in the absence of magnetic effects. *Journal of Applied Geophysics* **75**, 244–253.

Deceuster J., Etienne A., Robert T., Nguyen F. and Kaufmann O. 2014. A modified DOI-based method to statistically estimate the depth of investigation of dc resistivity surveys. *Journal of Applied Geophysics* **103**, 172–185.

Dietrich J.B. and Mitchell G. 2011. Geotechnical investigation Taxiway A, Iqaluit Airport (CYFB) Iqaluit, Nunavut. Peto MacCallum Ltd., 11KF074 for Genivar Inc.

Farquharson C.G. and Oldenburg D.W. 1998. Non-linear inversion using general measures of data misfit and model structure. *Geophysical Journal International* **134**, 213–227.

Fortier R., LeBlanc A.-M., Allard M., Buteau S. and Calmels F. 2008. Internal structure and conditions of permafrost mounds at Umiujaq in Nunavik, Canada, inferred from field investigation and electrical resistivity tomography. *Canadian Journal of Earth Sciences* **45**, 367–387.

Friedel S. 2003. Resolution, stability and efficiency of resistivity tomography estimated from a generalized inverse approach. *Geophysical Journal International* **153**, 305–316.

Groom D. 2008. Common misconceptions about capacitively-coupled resistivity (CCR): What it is and how it works. *Symposium on the Application of Geophysics to Environmental and Engineering Problems*, 1345–1350.

Grimm R.E., Stillman D.E., Dec S.F. and Bullock M.A. 2008. Low-frequency electrical properties of polycrystalline saline ice and salt hydrates. *Journal of Physical Chemistry B* **112**, 15382–15390.

Hauck C. 2013. New Concepts in Geophysical Surveying and Data Interpretation for Permafrost Terrain. *Permafrost and Periglacial Processes* **24**, 131–137.

Hauck C., Guglielmin M., Isaksen K. and Vonder Mühll D. 2001. Applicability of frequency-domain and time-domain electromagnetic methods for mountain permafrost studies. *Permafrost and Periglacial Processes* **12**, 39–52.

Hayashi M. 2004. Temperature-electrical conductivity relation of water for environmental monitoring and geophysical data inversion. *Environmental Monitoring and Assessment* **96**, 119–128.

Heginbottom J.A., Dubreuil M.H. and Harker P.T. 1995. Canada, Permafrost. In: *National Atlas of Canada*, *5th edition*, Plate 2.1, MCR 4177.

Hoekstra P. 1978. Electromagnetic methods for mapping shallow permafrost. *Geophysics* **43**, 782–787.

Hoekstra P., Sellmann P.V. and Delaney A. 1975. Ground and airborne resistivity surveys of permafrost near Fairbanks, Alaska. *Geophysics* **40**, 641–656.

King M.S. 1977. Acoustic velocities and electrical properties of frozen sandstones and shales. *Canadian Journal of Earth Sciences* **14**, 1004–1013.

King M.S., Zimmerman R.W. and Corwin R. F. 1988. Seismic and electrical properties of unconsolidated permafrost. *Geophysical Prospecting* **36**, 349–364.

Klein K.A. and Santamarina J.C. 2003. Electrical conductivity in soils: Underlying phenomena. *Journal of Environmental and Engineering Geophysics* **8**, 263–273.

Knapik D.J. and Hanna A.J. 1998. Foundation soils investigation, settlement of Apron III extension, Iqaluit Airport, Iqaluit, NT. AGRA Earth & Environmental Ltd. for the Government of the Northwest Territories, Department of Transportation.

Knight R.J. and Endres A.L. 2005. An introduction to rock physics principles for near-surface geophysics. In: *Near-Surface Geophysics* (ed D.K. Butler), 31–70. Society of Exploration Geophysicists.

Kuras O., Beamish D., Meldrum P.I. and Ogilvy R.D. 2006. Fundamentals of the capacitive resistivity technique. *Geophysics* **71**, G135–G152.

Larochelle Y.P. and Haché J.G.A.R. 1991. Geotechnical study, Alpha Taxiway, Iqaluit Airport. Jacques Whitford Ltd. for Public Works Canada.

LeBlanc A.-M., Mathon-Dufour V., Allard M., Oldenborger G.A., Short N., L'Hérault E. and Sladen W.E. 2013. Permafrost characterization at the Iqaluit International Airport, Nunavut, in support of decision-making and planning. Canada-Nunavut Geoscience Office, Summary of Activities 2012, 131–142.

LeBlanc A.-M., Oldenborger G.A., Sladen W.E. and Allard M. 2015. Infrastructure and climate warming impacts on ground thermal regime, Iqaluit International Airport, southern Baffin Island, Nunavut. Canada-Nunavut Geoscience Office, Summary of Activities 2014, 119–132.

Loke M.H., Acworth I. and Dahlin T. 2003. A comparison of smooth and blocky inversion methods in 2D electrical imaging surveys. *Exploration Geophysics* **34**, 182–187.

Loke M.H., Chambers J.E., Rucker D.F., Kuras O. and Wilkinson P.B. 2013. Recent developments in the direct-current geoelectrical imaging method. *Journal of Applied Geophysics* **95**, 135–156.

Marescot L., Loke M.H., Chapellier D., Delaloye R., Lambiel C. and Reynard E. 2003. Assessing reliability of 2D resistivity imaging in mountain permafrost studies using the Depth of Investigation index method. *Near Surface Geophysics* **1**, 57–67.

Mathon-Dufour V. 2014. Caractérisation du pergélisol en vue de la réfection et de l'adaptation aux changements climatiques de l'aéroport d'Iqaluit, Nunavut. MSc Thesis, Université Laval.

McNeil J.D. 1980a. Electrical conductivity of soils and rocks. Geonics Ltd., Technical Note TN-5.

McNeil J.D. 1980b. Electromagnetic terrain conductivity measurement at low induction numbers. Geonics Ltd., Technical Note TN-6.

Oldenburg D. and Li Y. 1999. Estimating depth of investigation in dc resistivity and IP surveys. *Geophysics* **64**, 403–416.

Oldenburg D.W. and Li Y. 2005. Inversion for applied geophysics: A tutorial. In: *Near-Surface Geophysics* (ed D.K. Butler), 89–150. Society of Exploration Geophysicists.

Oldenborger G.A. 2014. Comment on "The application of CCR and GPR to characterize ice conditions at Parsons Lake, Northwest Territories" by Angelopoulos et al. *Cold Regions Science and Technology* **100**, 68–70.

Oldenborger G.A., Stevens C.W. and Wolfe S.A. 2012. Electrical geophysics for assessing permafrost conditions along highway infrastructure. Proceedings of the Symposium on the Application of Geophysics to Environmental and Engineering Problems.

Oldenborger G.A. and LeBlanc A.-M. 2013. Capacitive resistivity inversion using effective dipole lengths for line antennas. *Journal of Applied Geophysics* **98**, 229–236.

Oldenborger G.A., LeBlanc A.-M. and Sladen W.E. 2014. Geophysical monitoring of permafrost conditions at Iqaluit International Airport, Nunavut. Canada-Nunavut Geoscience Office, Summary of Activities 2013, 129–137.

Oldenborger G.A., Routh P.S. and Knoll M.D. 2007. Model reliability for 3D electrical resistivity tomography: Application of the volume of investigation index to a time-lapse monitoring experiment. *Geophysics*, **72**, F167–F175.

Overduin P.P., Westermann S., Yoshikawa K., Haberlau T., Romonovsky V. and Wetterich S. 2012. Geoelectric observations of the degradation of nearshore submarine permafrost at Barrow (Alaskan Beaufort Sea). *Journal of Geophysical Research* **117**, F02004.

Palacky G.J. 1988. Resistivity characteristics of geologic targets. In: *Electromagnetic Methods in Applied Geophysics, Investigations in Geophysics* (ed M.N. Nabighian), 53–129. Society of Exploration Geophysicists.

Ross N., Brabham P.J., Harris C. and Christiansen H.H. 2007. Internal structure of open system pingos, Adventdalen, Svalbard: The use of resistivity tomography to assess ground-ice conditions. *Journal of Environmental and Engineering Geophysics* **12**, 113–126.

Sartorelli A.N. and French R.B. 1982. Electro-magnetic induction methods for mapping permafrost along northern pipeline corridors. Proceedings of the Fourth Canadian Permafrost Conference.

Scott W.J. and Hunter J.A. 1977. Applications of geophysical techniques in permafrost regions. *Canadian Journal of Earth Sciences* **14**, 117–127.

Scott W.J., Sellmann P.V. and Hunter J.A. 1990. Geophysics in the study of permafrost. In: *Geotechnical and Environmental Geophysics* (ed W.J. Ward), 355–384. Society of Exploration Geophysicists.

Short N., LeBlanc A.-M., Sladen W., Oldenborger G., Mathon-Dufour V., and Brisco B. 2014. RADARSAT-2 DInSAR for ground displacement in permafrost terrain, validation from Iqaluit Airport, Baffin Island, Canada. *Remote Sensing of Environment* **141**, 40–51.

Sladen W.E., Dyke L.D. and Smith S.L. 2009. Permafrost at York Factory National Historic Site of Canada, Manitoba, Canada. Geological Survey of Canada, Current Research 2009-4.

Stummer P., Maurer H. and Green A.G. 2004. Experimental design: Electrical resistivity data sets that provide optimum subsurface information. *Geophysics* **69**, 120–139.

Supper R., Ottowitz D., Jochum B., Römer A., Pfeiler S., Kauer S., Keuschnig M. and Ita A. 2014. Geoelectrical monitoring of frozen ground and permafrost in alpine areas: field studies and considerations towards an improved measuring technology. *Near Surface Geophysics* 93–115.

Wolfe S.A., Stevens C.W., Gaanderse A.J. and Oldenborger G.A. 2014. Lithalsa distribution, morphology and landscape associations in the Great Slave Lowland, Northwest Territories, Canada. *Geomorphology* **204**, 302–313.

You Y., Yu Q., Pan X. and Guo L. 2013. Application of electrical resistivity tomography in investigating depth of permafrost base and permafrost structure in Tibetan Plateau. *Cold Regions Science and Technology* **87**, 19–26.

TABLES

Table 1. Observed electrical resistivities and approximate depths. Observations below the limit of model reliability are not included.

Site	Survey	Depth Range (m)	Map Unit	Interpretation	Resistivity (Ωm)	Resistivity* (Ωm)
A3	CR	0–5	GMd	Sand/gravel	1000–3000	1730
A3	CR	5+	Unidentified	Unknown	10–30	20
A07	CR/GR	0–5	Mn	Silt/sand/gravel	1000–3000	1730
A07	CR	0–5	Tb	Till	500–1500	870
A07	CR/GR	5+	Unidentified	Unknown	10–30	20
A07x	GR	0–8	Mn	Ice-rich silt/sand/gravel	5000–8000	6320
A10	GR	0–7	GMd	Sand/gravel	800–2000	1260
A10	GR	0–10	Polygon	Ice wedge	8000–10000	8940
A11	CR	0–3	GMd	Sand/gravel	800–1000	890
Runway	CR	4+	R	Bedrock	8000–20000	12650
Runway	CR	0–10+	GFp/GMd	Sand/gravel	800–3000	1550
Runway	CR	4+	Unidentified	Unknown	20–300	80
Taxi A	CR	0–6	Lv	Silt	50–200	100
Taxi A	CR	0–10+	GFp/GMd	Sand/gravel	800–1500	1100
Taxi A	CR	0–8	GMd	Ice-rich sand/gravel	5000–8000	6320
Taxi A	CR	4+	Unidentified	Unknown	5–50	20
Taxi B	CR	0–10+	Ap	Ice-rich sand/gravel	3000–10000	5480
Taxi B	CR	0–10+	GMd	Sand/gravel	1000–8000	2830
Taxi A	GR	1–10+	R	Bedrock	4000–16000	8000
Taxi A	GR	0–5	GMd	Ice-rich sand/gravel	2000–10000	4470
Taxi A	GR	0–3	GFp	Sand/gravel	1000–3000	1730
Taxi A	GR	0–7	Lv	Silt	15–30	20
Taxi A	GR	7–12	Lv	Silt/sand	50–100	70
Taxi A	GR	3–10+	Unidentified	Unknown	1–30	10

*Log-based mean

Table 2. Grain size, water content and pore-water conductivity for DH11-07 cutting samples.

Depth (m)	Sand (wt %)	Silt (wt %)	Clay (wt %)	Water (wt %)	Fluid Conductivity (20ºC, mS/m)	Approximate Salinity (g/L)
3.7	8.8	83.1	7.8	32.8	631	4.4
6.9	21.5	71.6	5.8	23.2	735	5.1
11.6	37.2	58.1	4.5	16.7	1234	8.6
Fresh Water*					10	0.1
Sea Water*					5000	35

*Palacky 1988

FIGURES

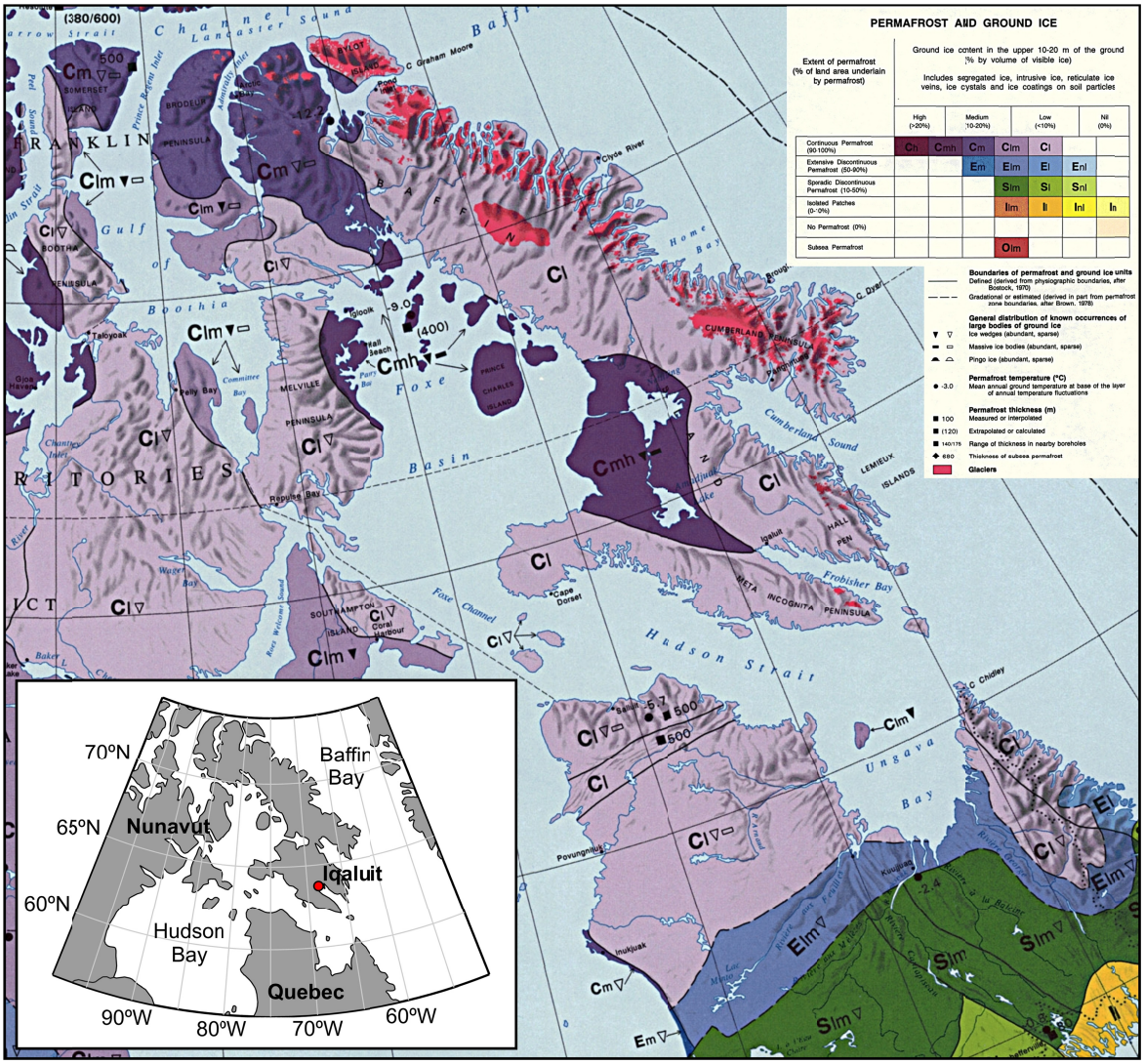

Figure 1. Permafrost and ground ice map of Baffin Island (Heginbottom et al. 1995). Iqaluit is located at the Head of Frobisher Bay (inset map).

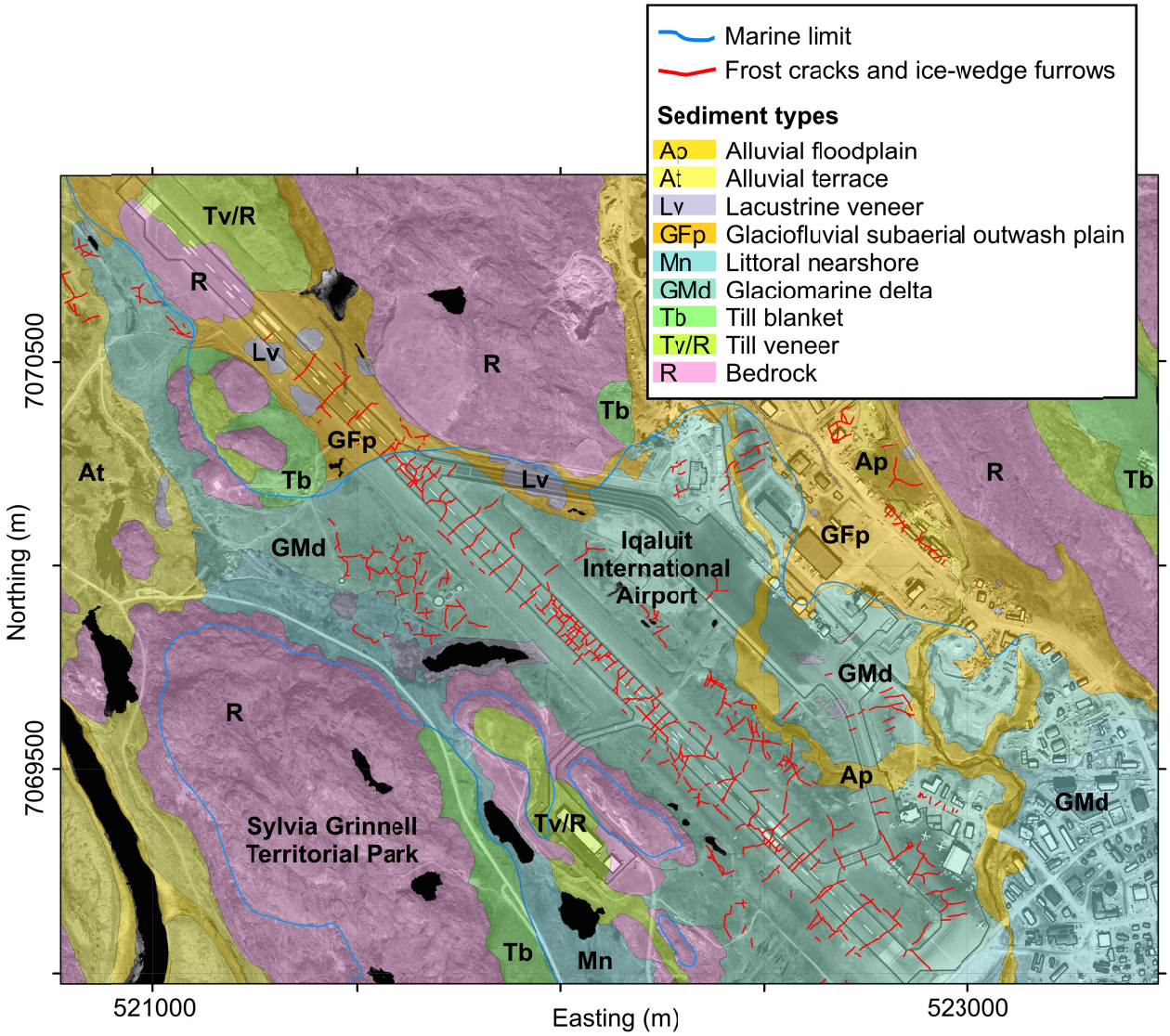

Figure 2. Surficial geology of the region around YFB. For a full description of sediment types, see Allard et al. (2012). QuickBird satellite image 25/07/2006, copyright DigitalGlobe Inc., all rights reserved.

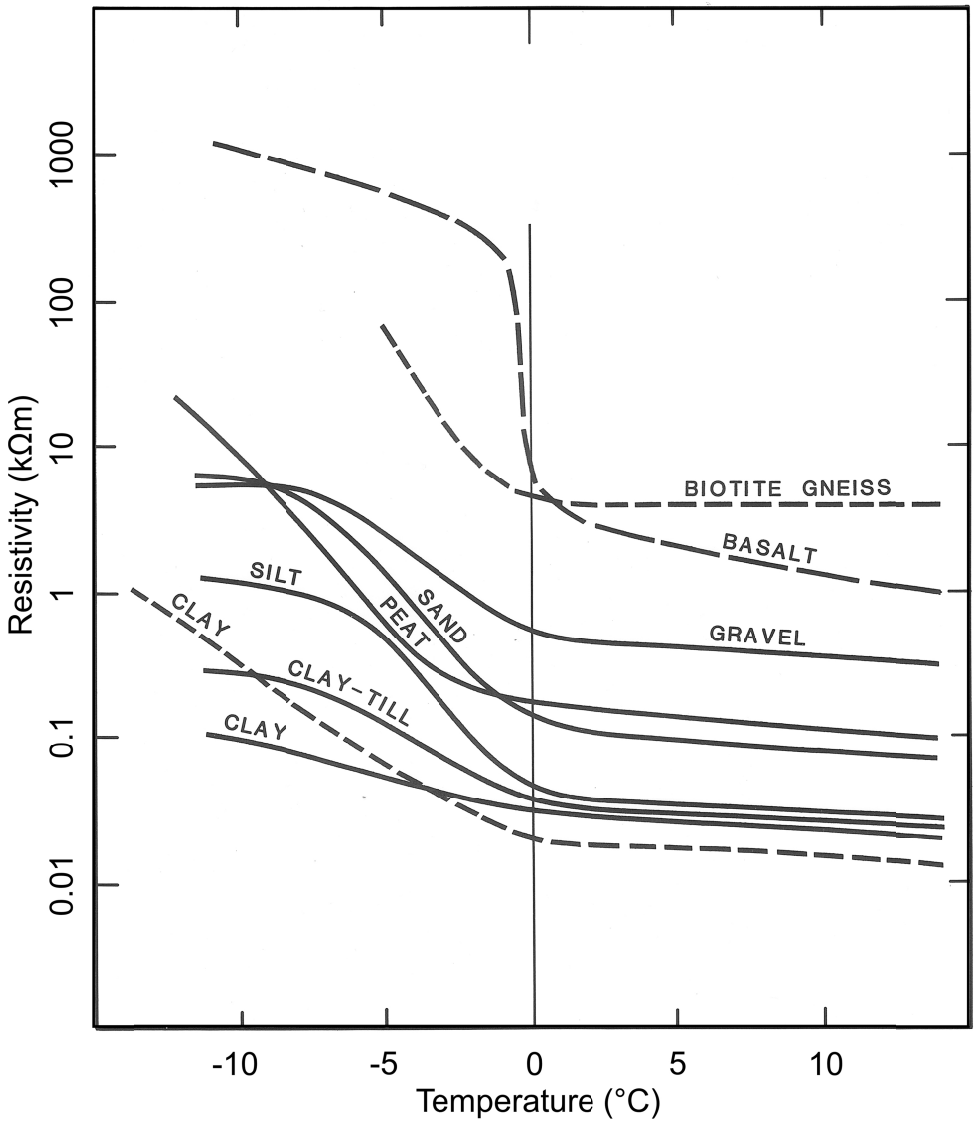

Figure 3. Electrical resistivity as a function of temperature for a variety of generic material types (Scott et al. 1990).

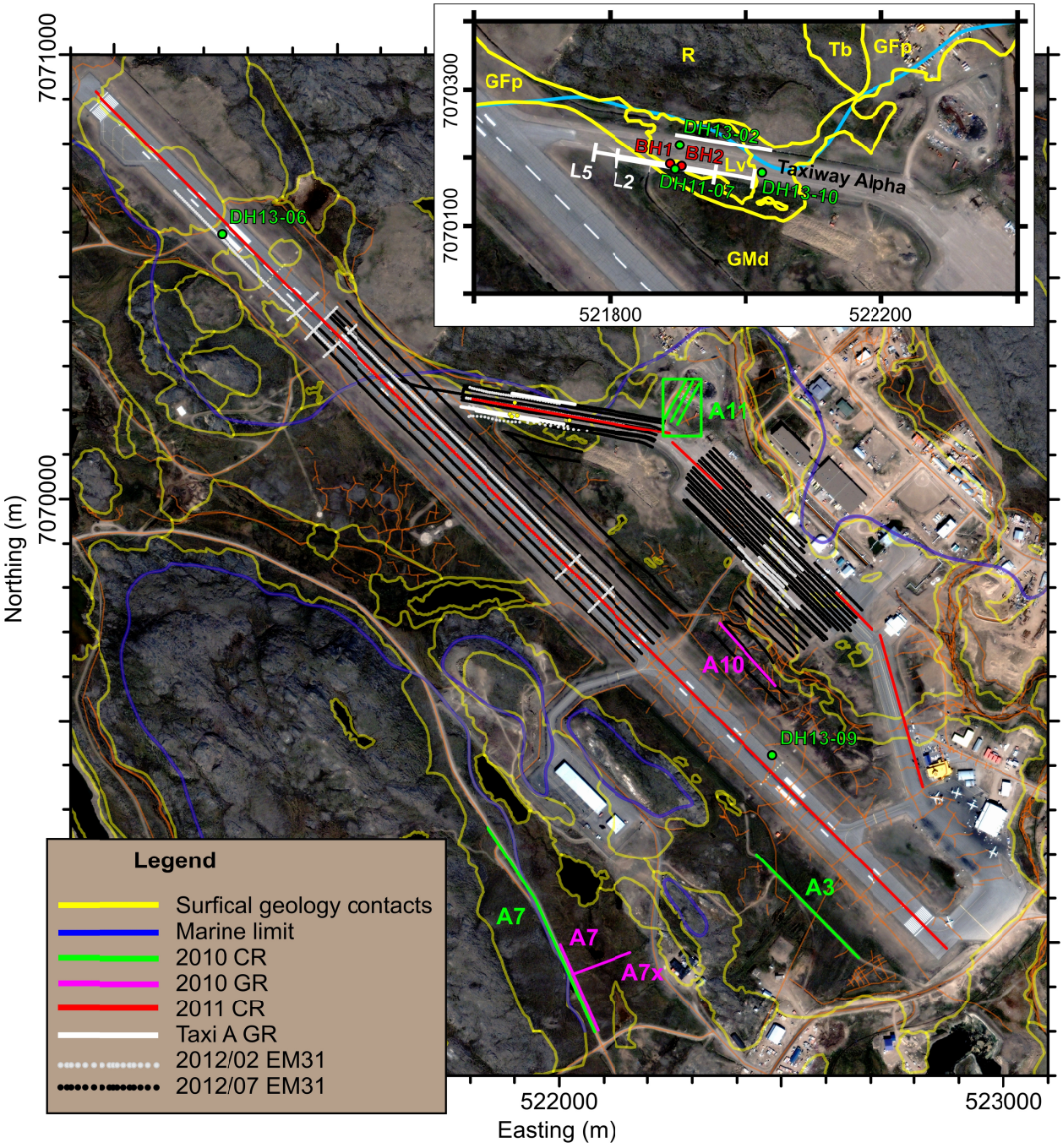

Figure 4. Locations of geophysical data collected by the GSC at YFB and in the vicinity from 2010 to 2013. Inset shows Taxiway Alpha. Worldview-1 satellite image 19/08/2008, copyright DigitalGlobe Inc., all rights reserved.

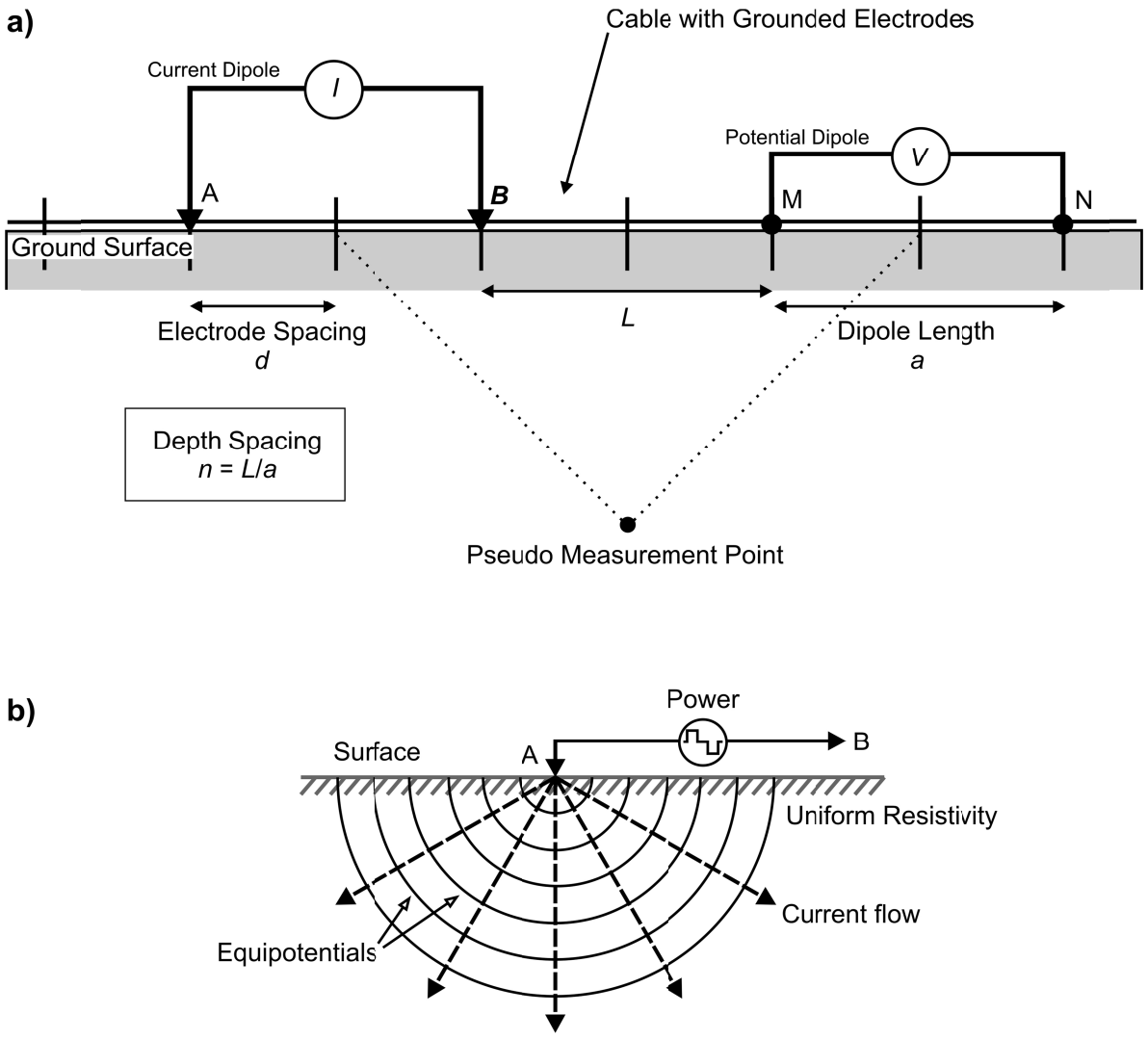

Figure 5. Schematic survey geometry for the galvanic resistivity experiment. a) Current and potential dipole lengths are integer multiples of the electrode spacing. Reciprocal measurements involve a reversal of the current and potential electrodes. The measurement dipoles are selected on the electrode cable via electronic switching. b) Current injection and resulting potential distribution for a point source and a homogeneeous halfspace.

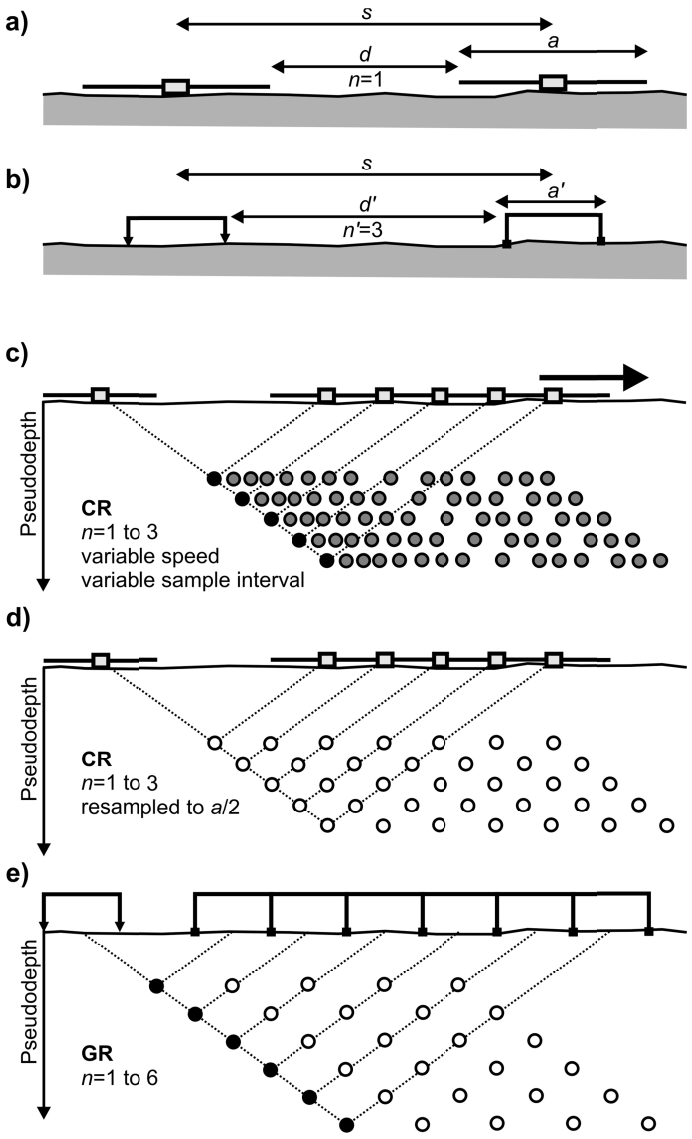

Figure 6. Schematic of in-line dipole-dipole CR survey geometry with line antennas. a) Physical antenna lengths and conventionally applied GR parameters of dipole length *a* and *n*-spacing. b) Hypothetical equivalent GR geometry with an effective dipole length of one-half the antenna length. c) Pseudodepth-distance data distribution for CR data where variable speed and constant sample frequency result in a variable sample interval. d) CR data resampled to a constant sample interval. e) GR data with fixed electrodes at an equivalent dipole length.

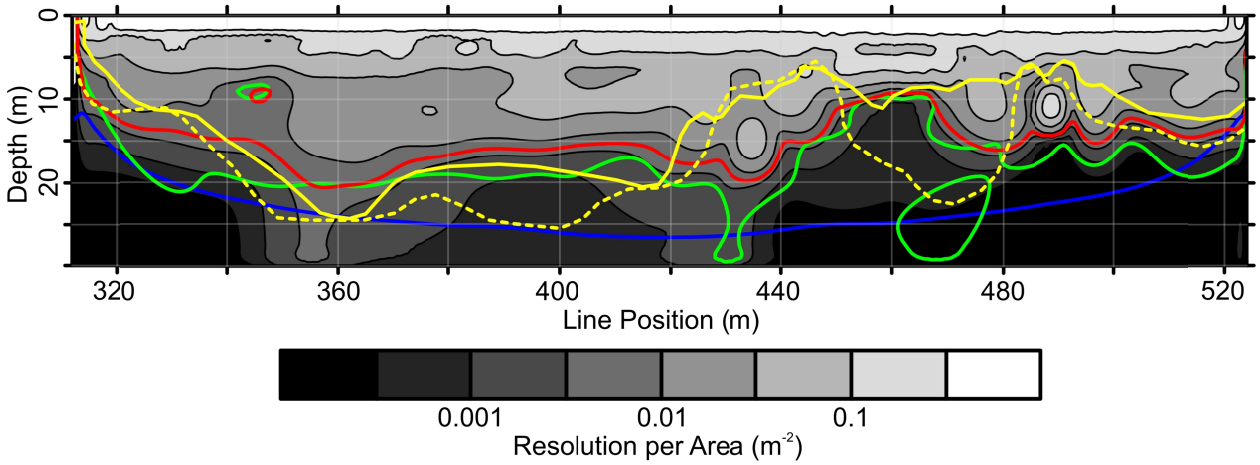

Figure 7. Model resolution matrix diagonals for inversion of A07 GR data. Red line: 0.5% maximum resolution per area. Green line: 0.5% maximum resolution per area with no reference model. Blue line: 0.5% maximum resolution per area for homogeneous model. Yellow line: 0.2 depth of investigation index. Yellow dashed line: 0.2 depth of investigation index with insufficient smallness.

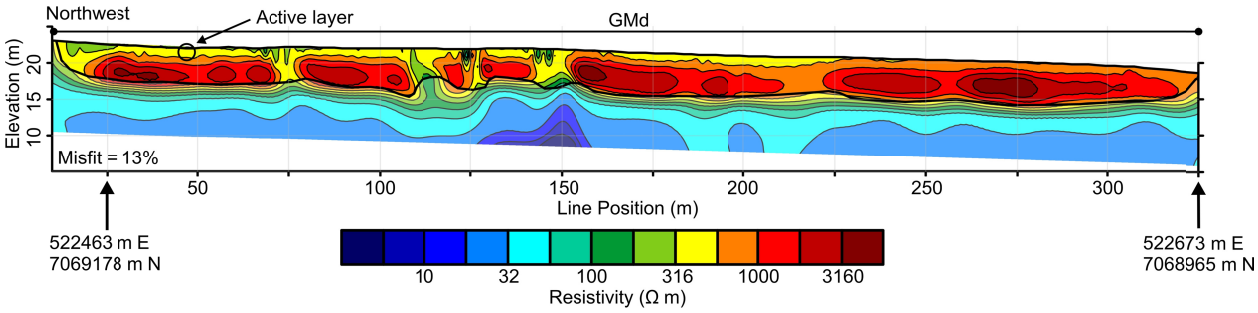

Figure 8. Electrical resistivity model recovered from inversion of $p = 0.8$ corrected A03 CR data acquired with 5 m antenna length (August, 2010). The conductive anomaly at approximately 140 m line position is coincident with signage for underground high voltage transmission infrastructure. Heavy black line indicates limit of model reliability. Vertical exaggeration: 1.5 times.

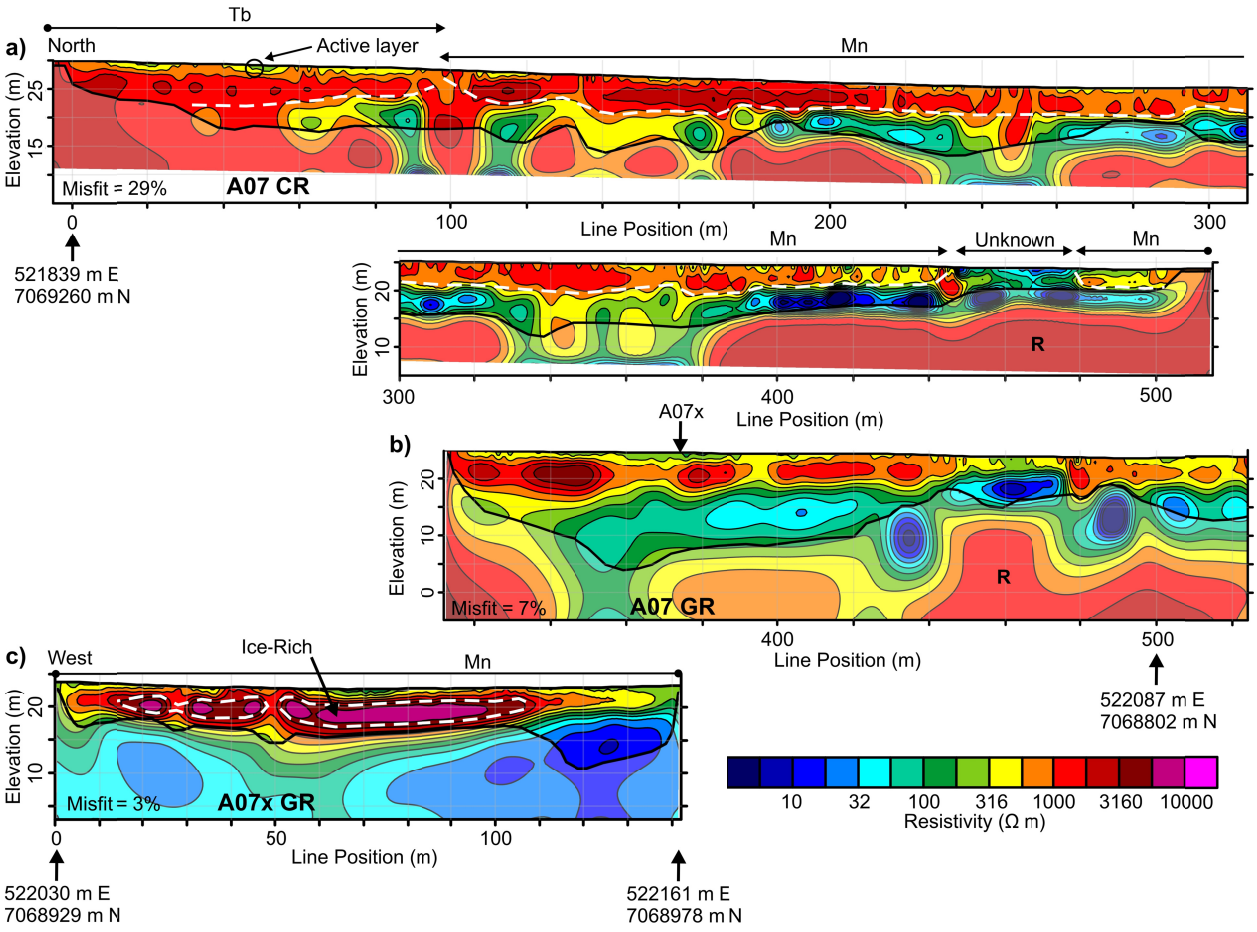

Figure 9. Electrical resistivity model recovered from a) inversion of $p = 0.8$ corrected A07 CR data acquired with 5 m antenna length, b) A07 GR data acquired with 3 m electrode spacing and c) A07x GR data acquired with 2 m electrode spacing (August, 2010). Heavy black line indicates limit of model reliability. Vertical exaggeration: 1.5 times.

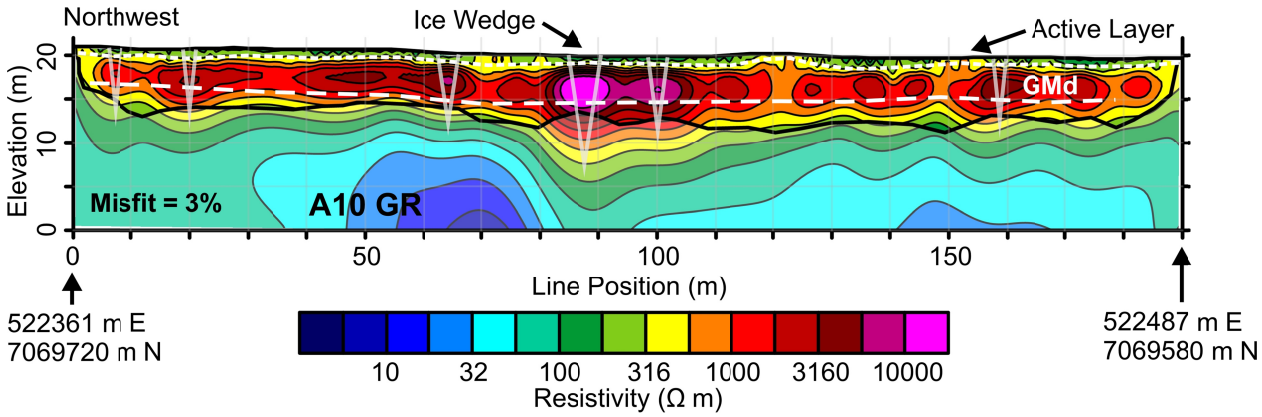

Figure 10. Electrical resistivity model recovered from inversion of A10 GR data acquired with 2 m electrode spacing (August, 2010). Resistive anomalies co-located with polygonal furrows are interpreted as ice wedges illustrated schematically (not to scale). Heavy black line indicates limit of model reliability. Vertical exaggeration: 1.5 times.

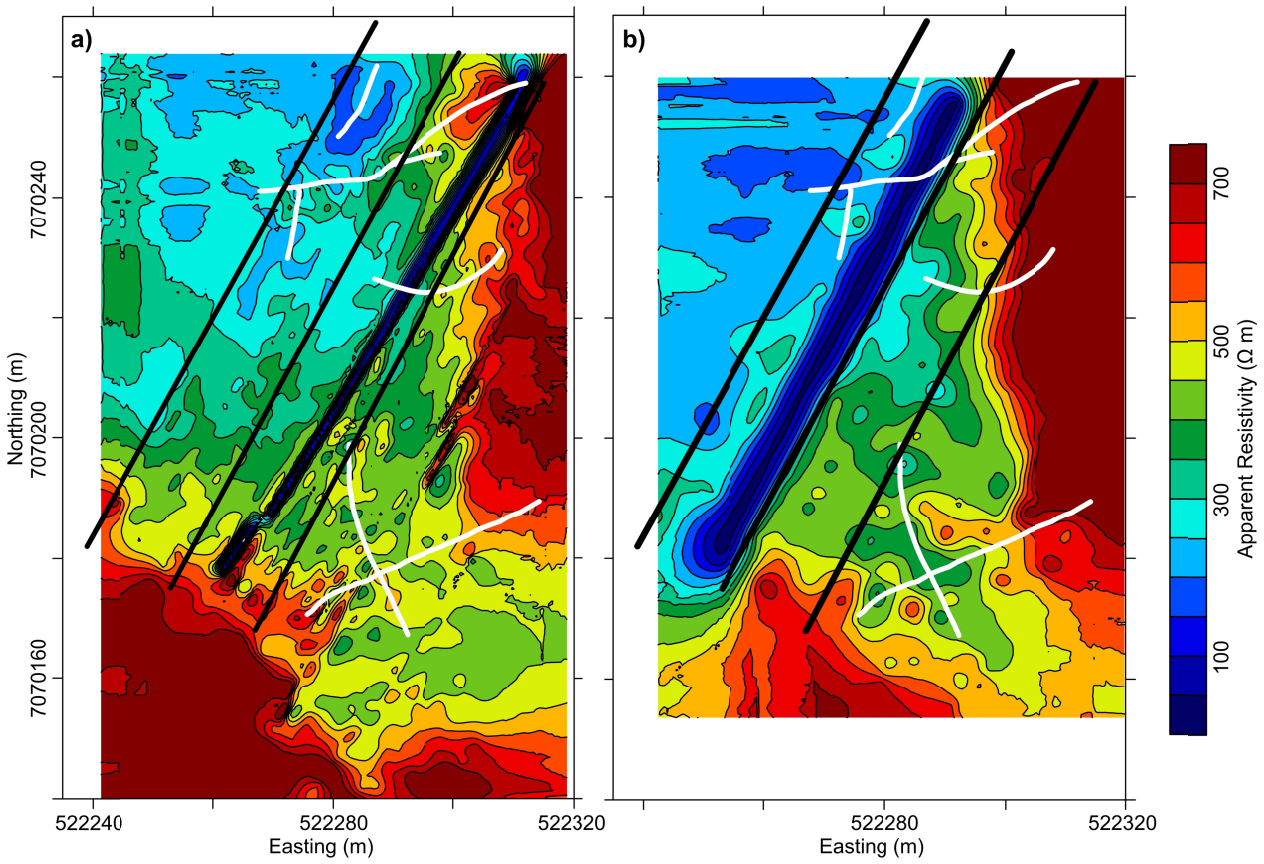

Figure 11. Apparent electrical resistivity derived from $p = 0.8$ corrected A11 CR data acquired with 5 m antenna length at nominal exploration depths of a) 1.5 m and b) 3 m (August, 2010). White lines represent frost crack features of Allard et al. (2012). Black lines indicate locations of A11 CR depth data (Fig. 12).

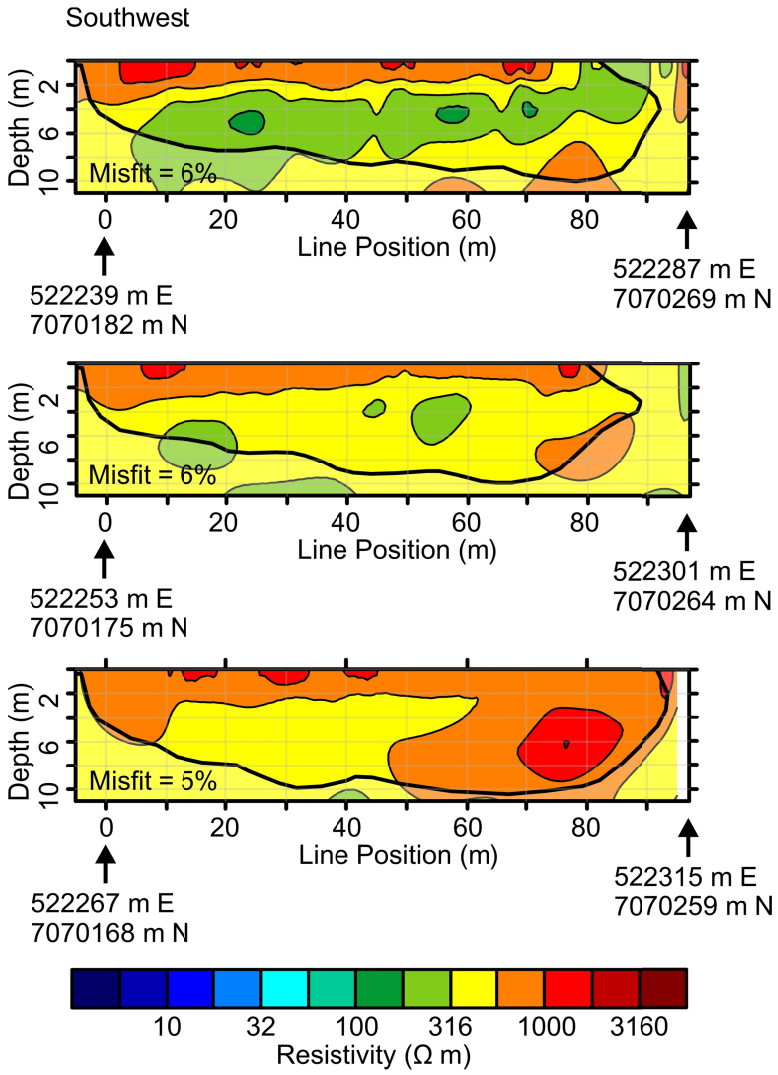

Figure 12. Electrical resistivity model recovered from inversion of $p = 0.8$ corrected A11 CR data acquired with 5 m antenna length (August, 2010). Heavy black line indicates limit of model reliability. Vertical exaggeration: 2 times.

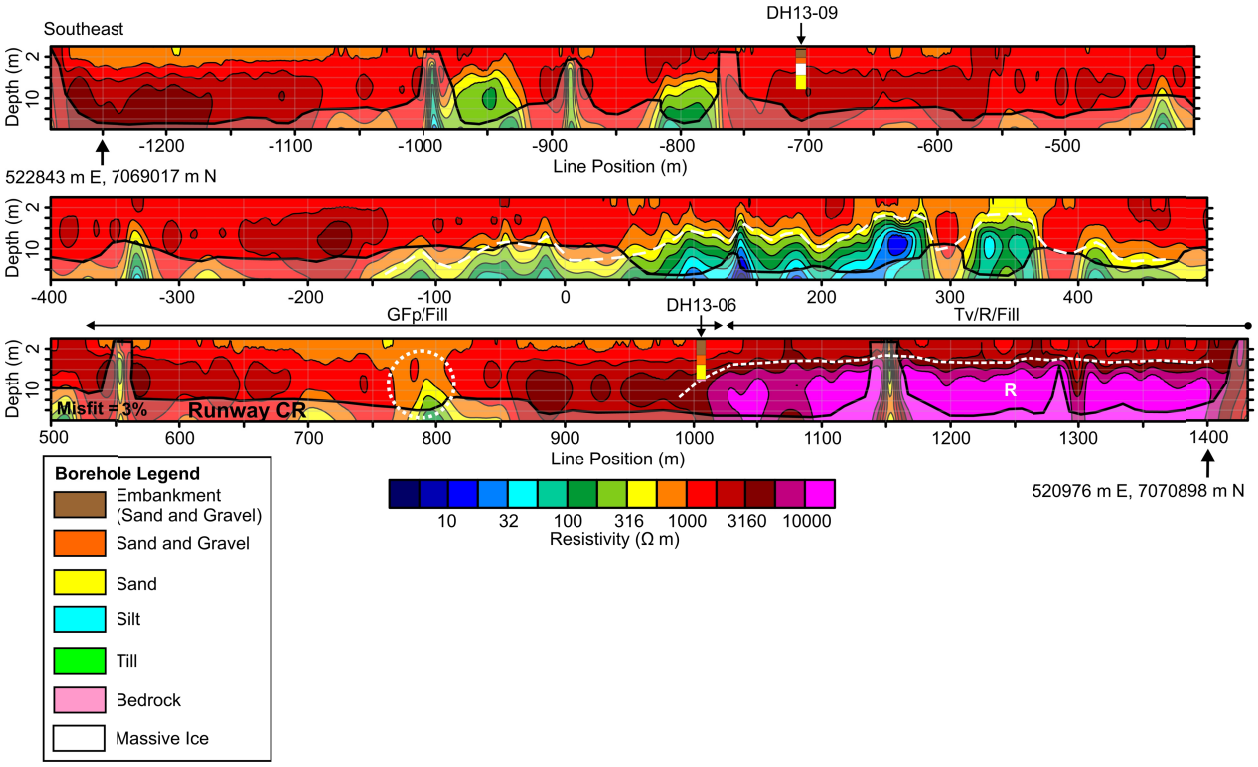

Figure 13. Electrical resistivity models recovered from inversion of $p = 0.8$ corrected CR data acquired with 10 m antenna length along Runway 17/35 (July, 2011). Heavy black line indicates limit of model reliability. Schematic borehole stratigraphy for DH13-06 and DH13-09 from Mathon-Dufour (2014). Vertical exaggeration: 4 times.

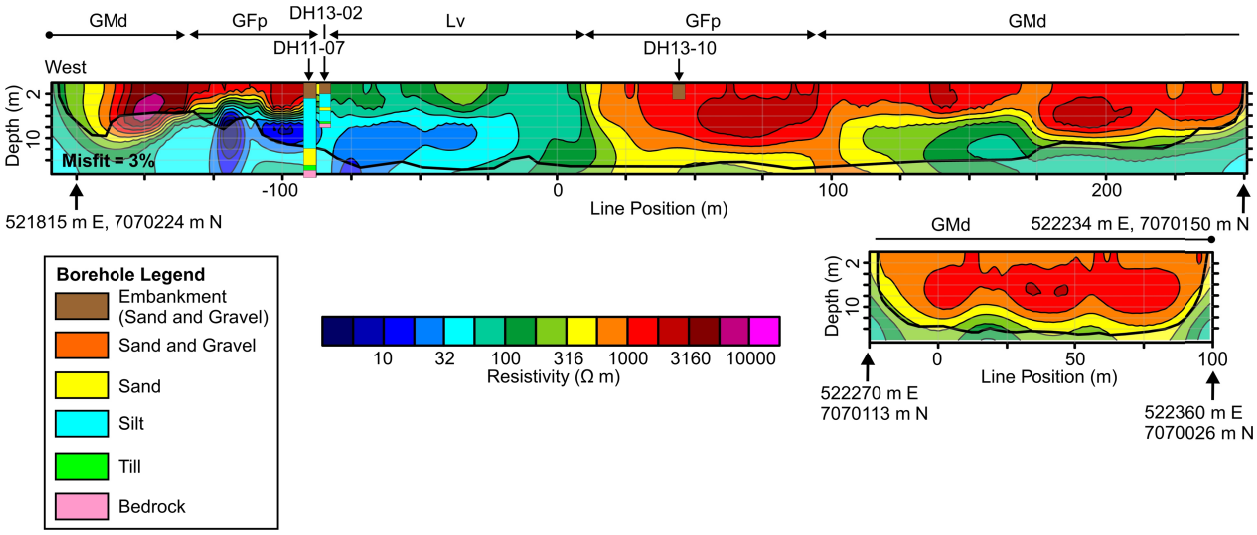

Figure 14. Electrical resistivity models recovered from inversion of $p = 0.8$ corrected CR data acquired with 10 m antenna length along Taxiway A (July, 2011). Heavy black line indicates limit of model reliability. Schematic borehole stratigraphy for DH13-02 and DH13-10 from Mathon-Dufour (2014). Boreholes DH11-07 and DH13-02 are approximately 20 m and 10 m off-line, respectively. Vertical exaggeration: 2 times.

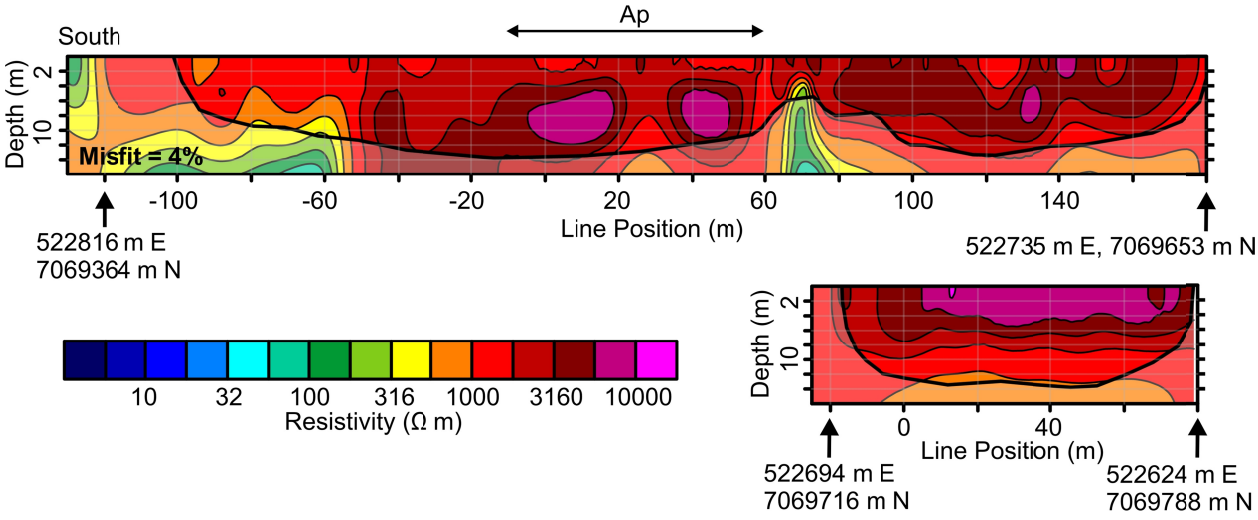

Figure 15. Electrical resistivity models recovered from inversion of $p = 0.8$ corrected CR data acquired with 10 m antenna length along Taxiway B (July, 2011). Heavy black line indicates limit of model reliability. Vertical exaggeration: 2 times.

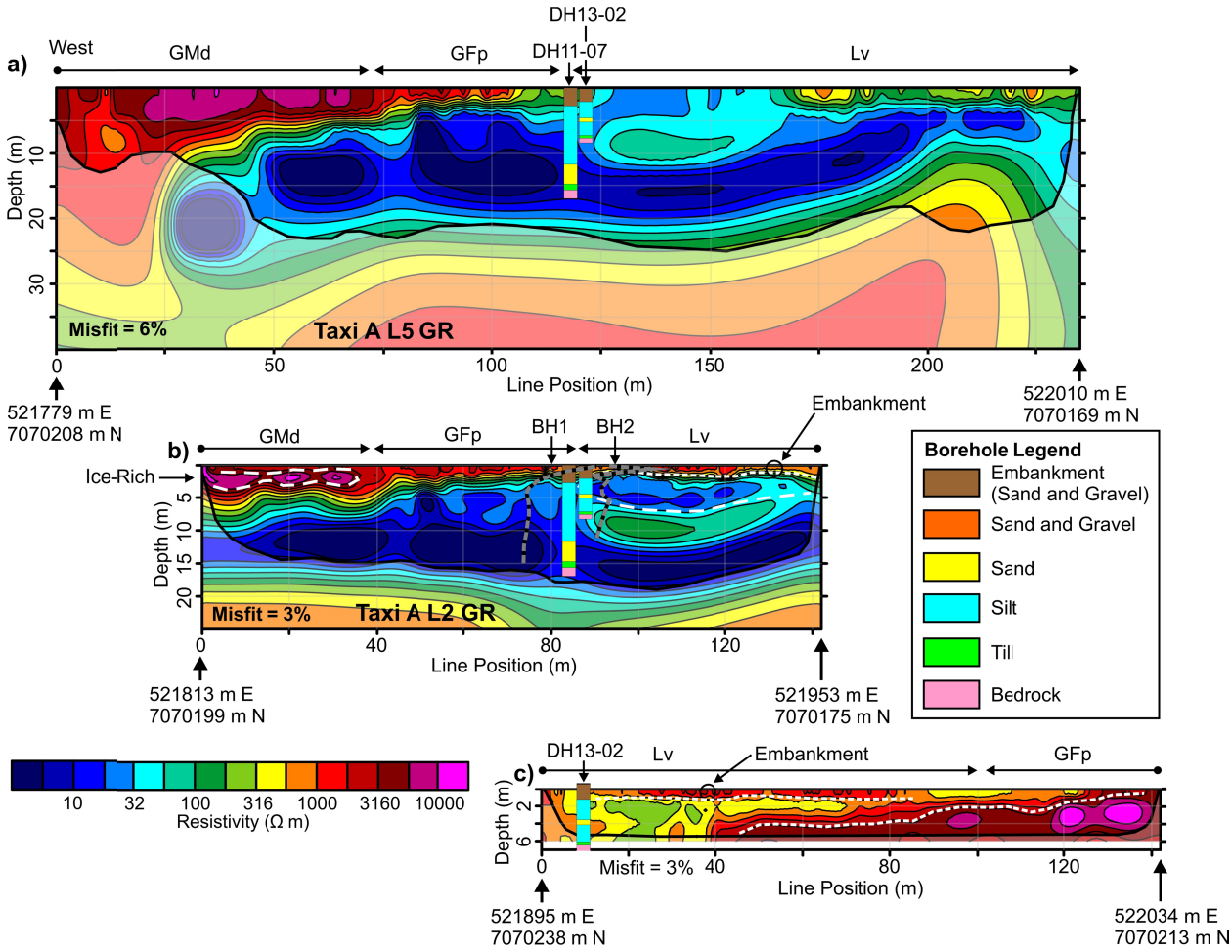

Figure 16. Electrical resistivity models recovered from inversion GR data along the southern edge of Taxiway A with a) surface electrodes at 5m spacing (July, 2012) and b) installed electrodes at 2 m spacing (August, 2012). Dashed curves show temperature and dielectric constant profiles for BH1 and BH2 respectively (Oldenborger et al. 2014). Heavy black line indicates limit of model reliability; vertical exaggeration 1.5 times. c) Electrical resistivity model recovered from inversion GR data along the northern shoulder of Taxiway A with surface electrodes at 2 m spacing (August, 2014). Heavy black line indicates limit of model reliability; vertical exaggeration: 2 times. Borehole stratigraphy for DH13-02 from Mathon-Dufour (2014).

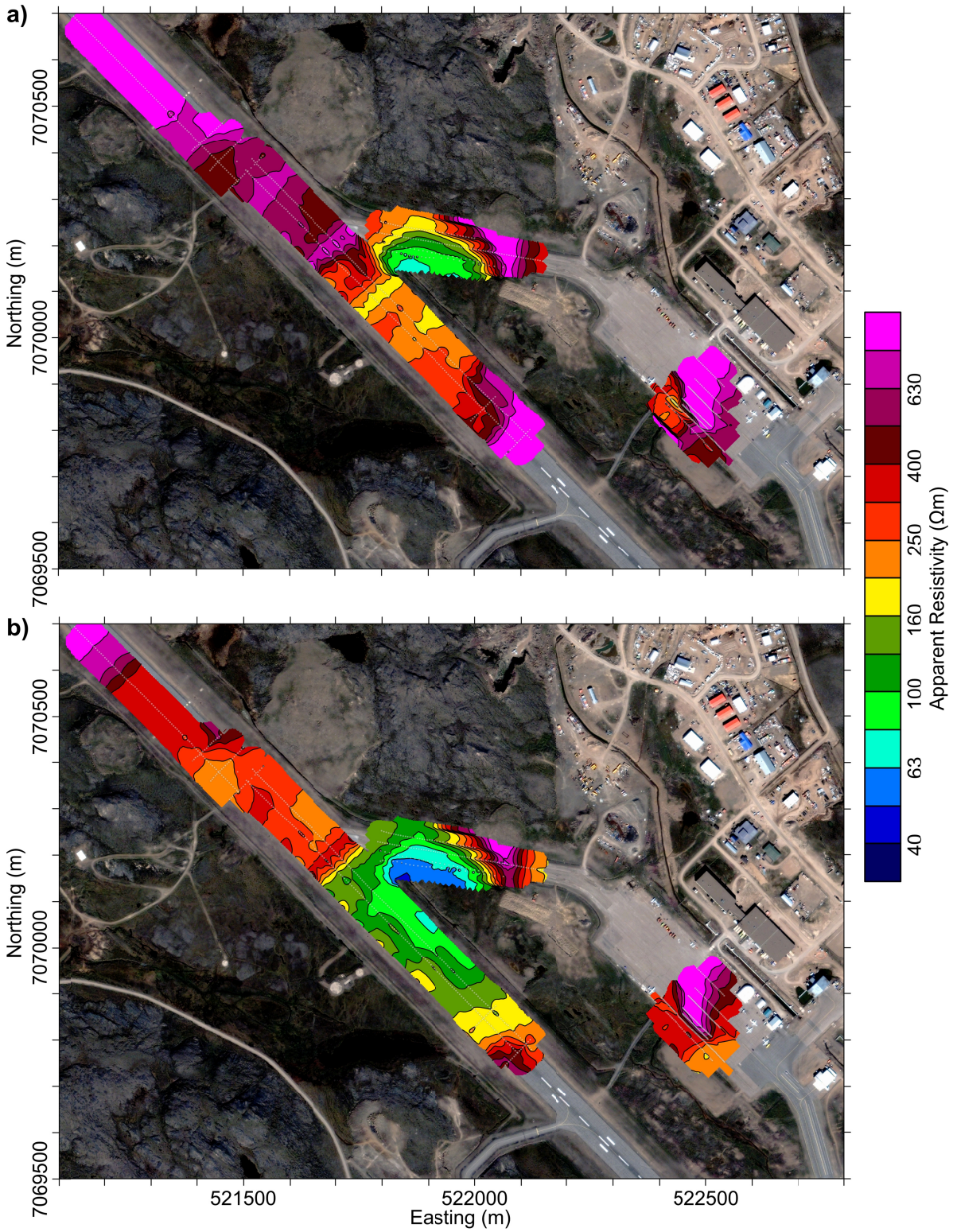

Figure 17. EM31 apparent resistivity data collected in February, 2012. a) Horizontal dipole mode with an approximate exploration depth of 3 m. b) Vertical dipole mode with an approximate exploration depth of 6 m. QuickBird satellite image 25/07/2006, copyright DigitalGlobe Inc., all rights reserved.

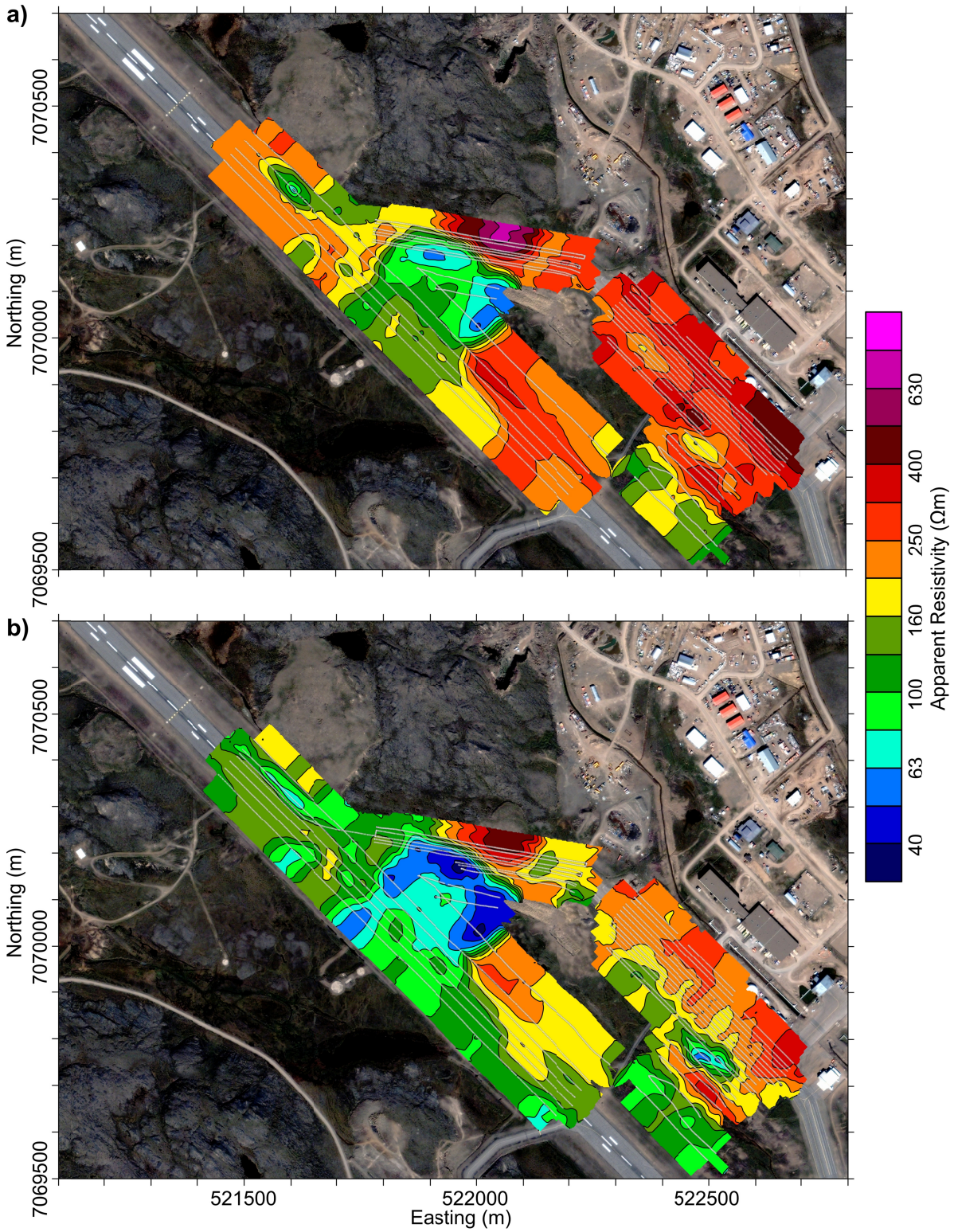

Figure 18. EM31 apparent resistivity data collected in July, 2012. a) Horizontal dipole mode with an approximate exploration depth of 3 m. b) Vertical dipole mode with an approximate exploration depth of 6 m. QuickBird satellite image 25/07/2006, copyright DigitalGlobe Inc., all rights reserved.

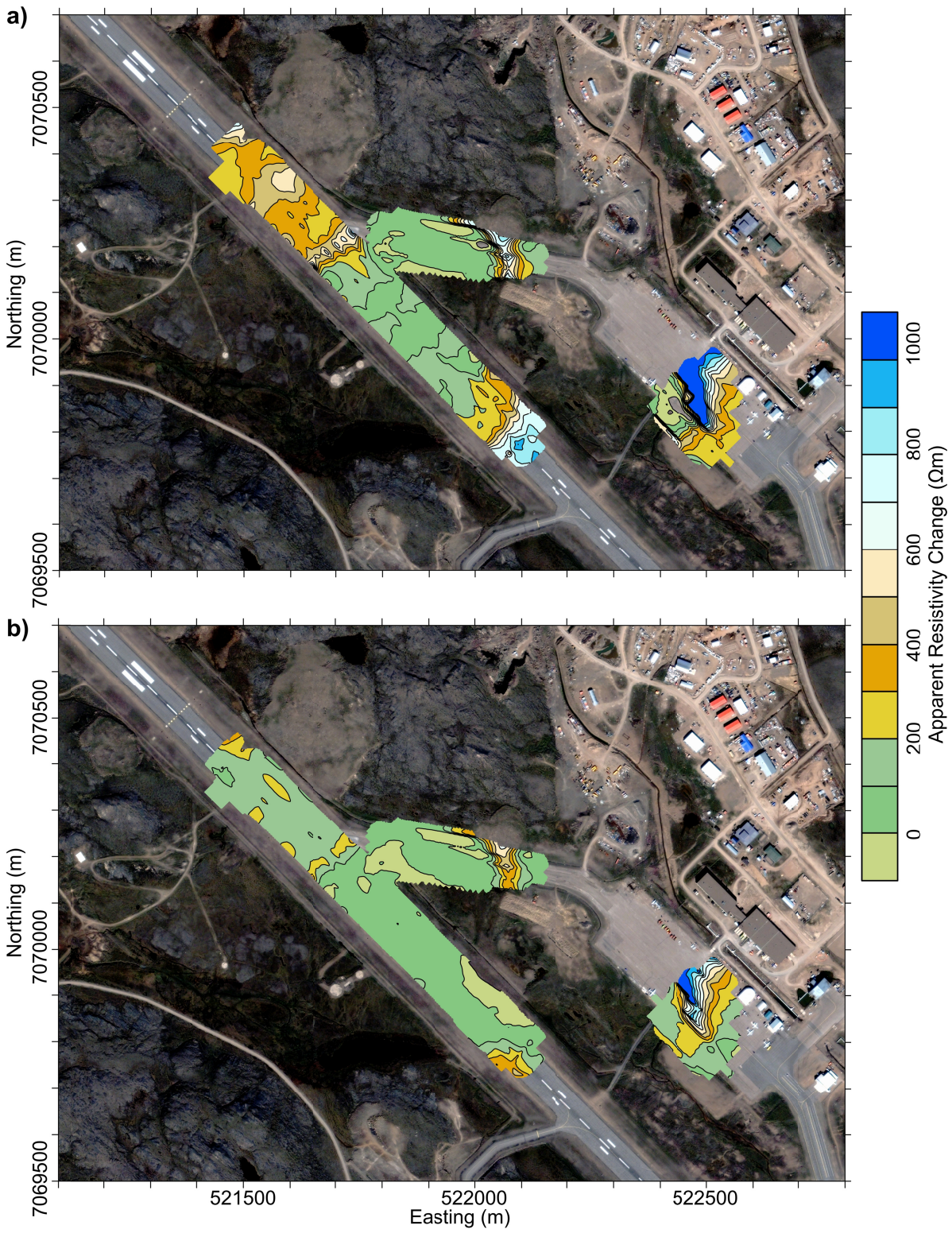

Figure 19. Change in EM31 apparent resistivity data from winter to summer. a) Horizontal dipole mode with an approximate exploration depth of 3 m. b) Vertical dipole mode with an approximate exploration depth of 6 m. QuickBird satellite image 25/07/2006, copyright DigitalGlobe Inc., all rights reserved.

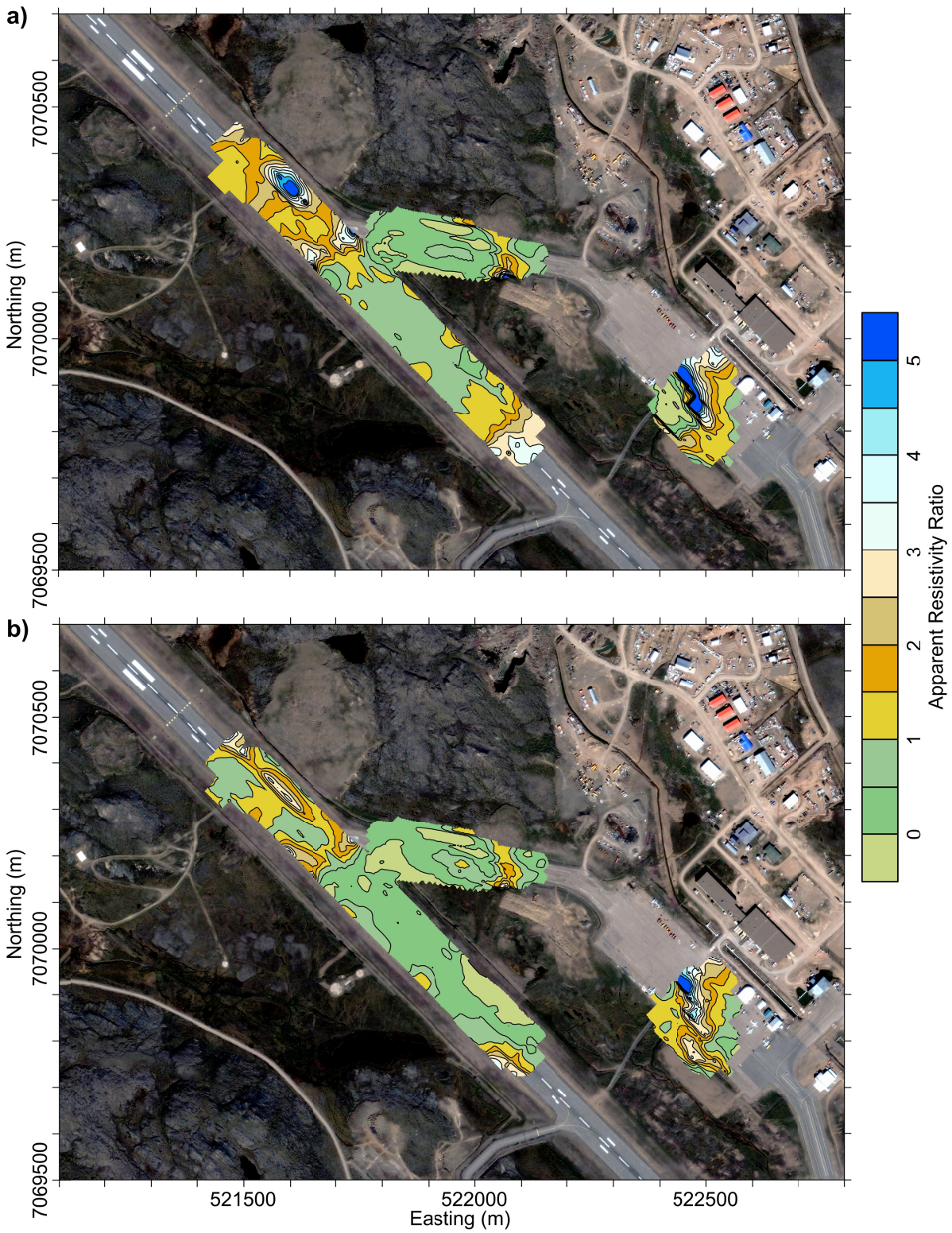

Figure 20. Change in EM31 apparent resistivity data from winter to summer normalized to summer conditions. a) Horizontal dipole mode with an approximate exploration depth of 3 m. b) Vertical dipole mode with an approximate exploration depth of 6 m. QuickBird satellite image 25/07/2006, copyright DigitalGlobe Inc., all rights reserved.

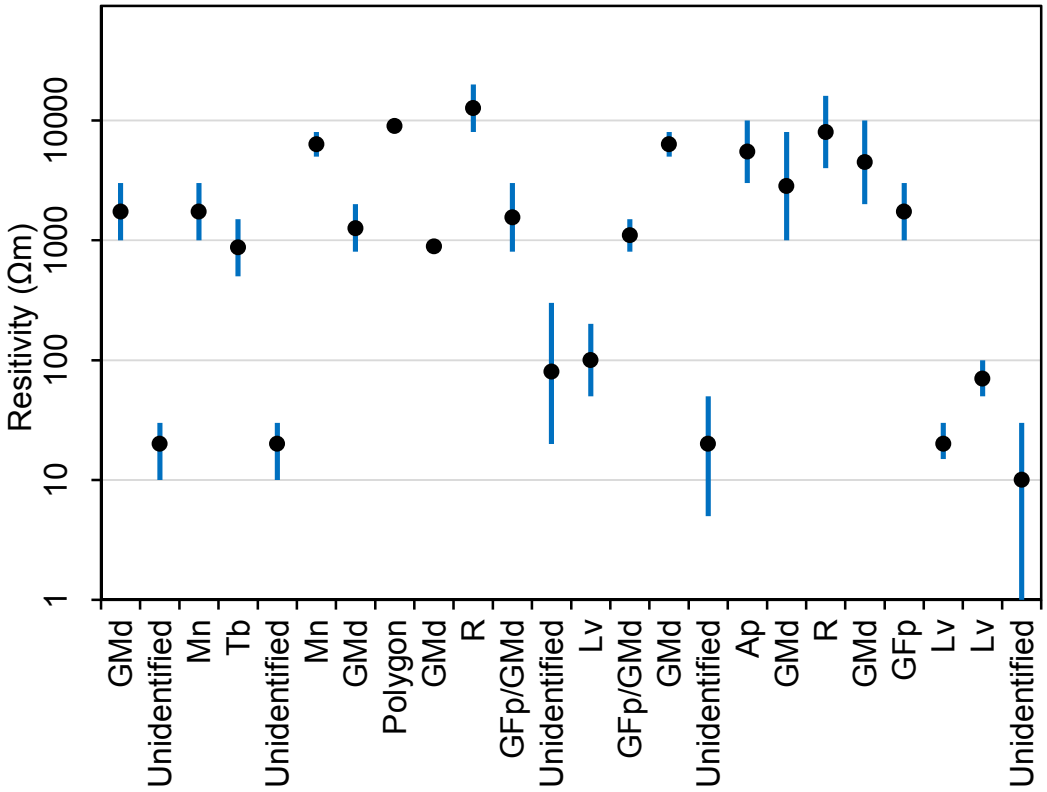

Figure 21. Observed resistivity distribution in site order as per Table 1. Blue lines indicate resistivity range and black dots indicate log-based mean.

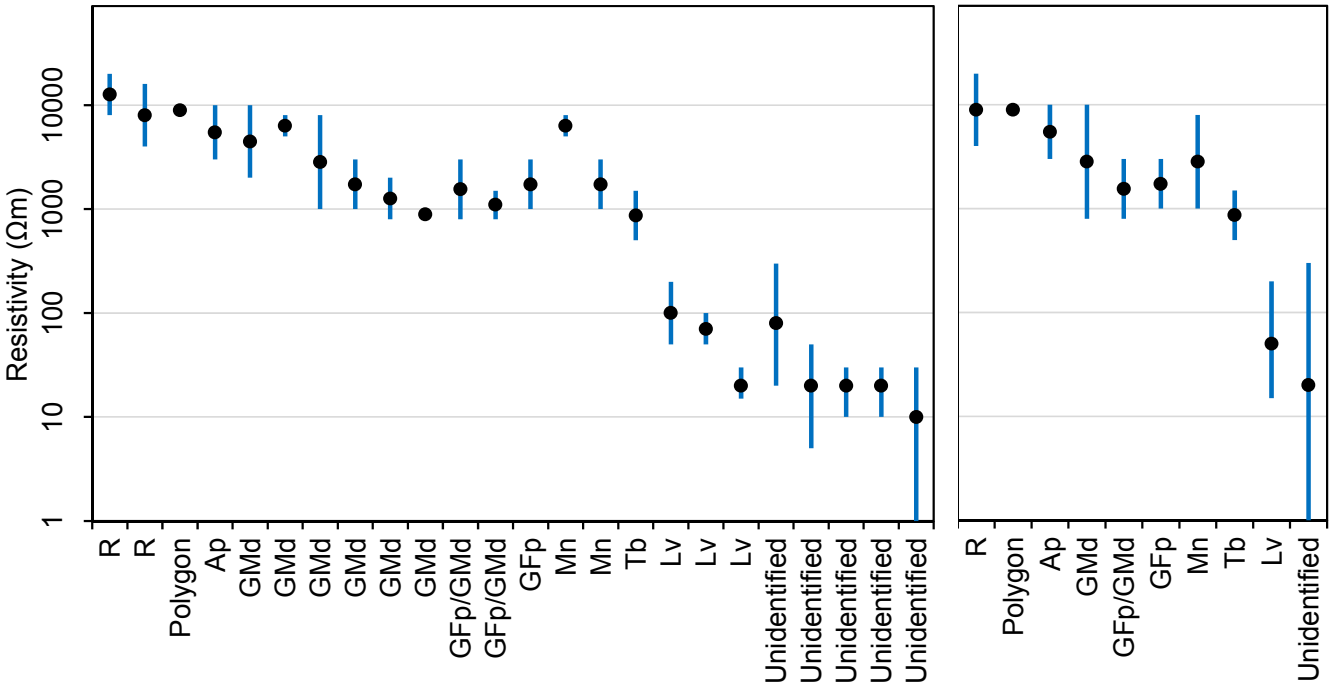

Figure 22. Observed resistivity distribution ordered by map units on a site-by-site basis (left) and grouped regionally (right) in approximate order of decreasing resistivity. Blue lines indicate resistivity range and black dots indicate log-based mean.

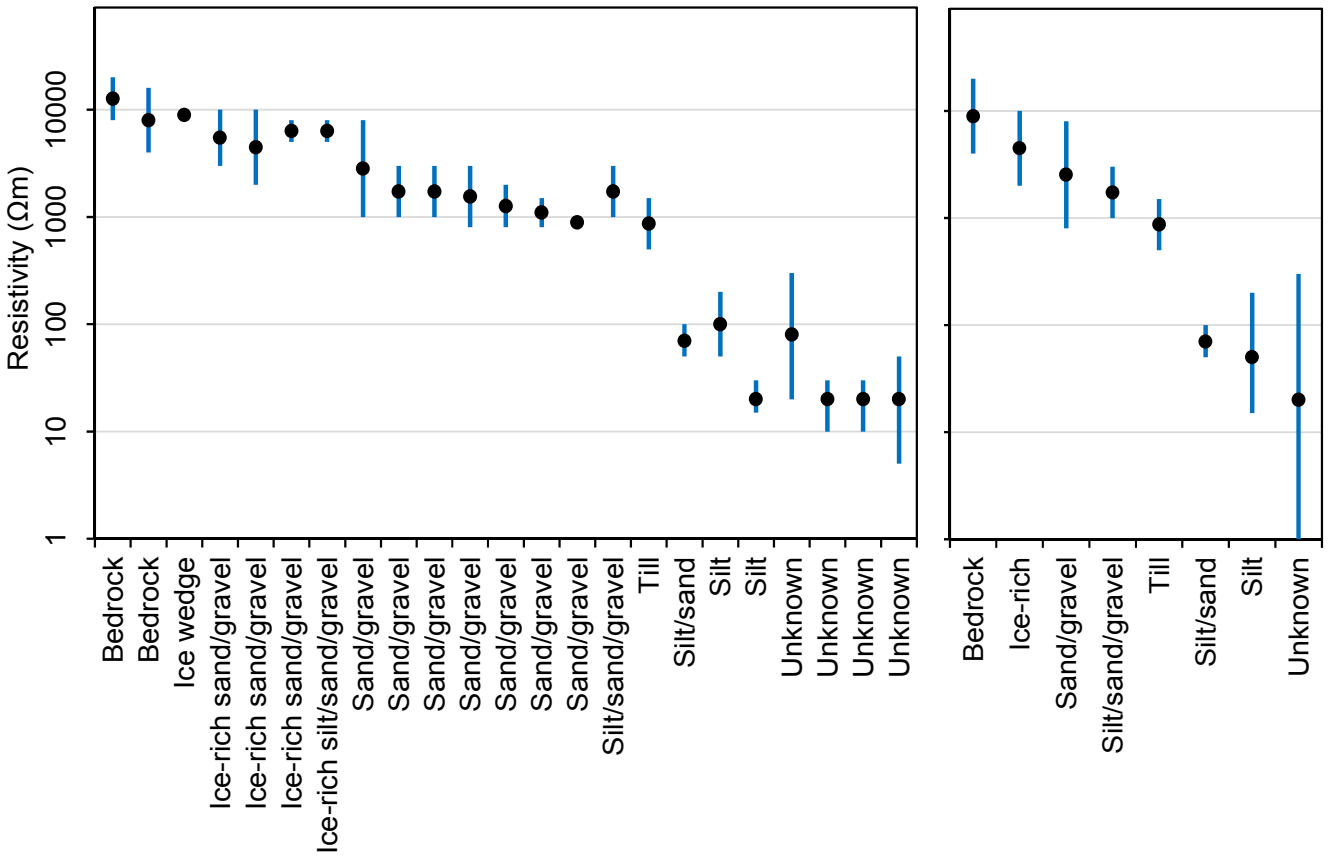

Figure 23. Observed resistivity distribution ordered by interpreted sediment type on a site-by-site basis (left) and grouped regionally (right) in approximate order of decreasing resistivity. Blue lines indicate resistivity range and black dots indicate log-based mean.

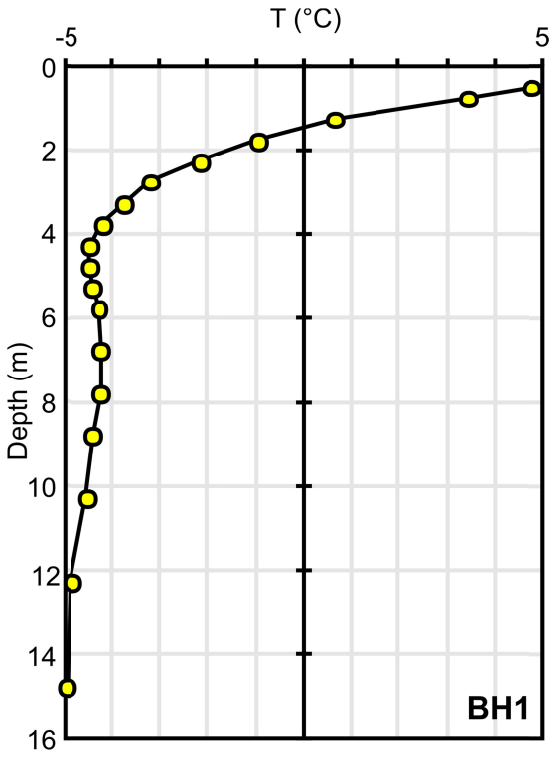

Figure 24. Temperature as a function of depth in BH1 on 14/07/2013 (Oldenborger et al. 2014).